# Chapter 4. Kolsky Compression Bar Experiments on Soft Materials

In this chapter, we present Kolsky-bar techniques modified for soft material characterization in compression. Soft materials typically have low strength, stiffness, and wave impedance, which make it challenging to obtain accurate stress-strain responses at high strain rates. The challenges in characterizing soft materials are introduced in this chapter. Solutions in regard to achieving stress equilibrium, generating proper pulse shapes and sensing low-amplitude forces are then presented. Experimental design for soft material characterization is illustrated with example materials that include PMMA, rubber and rubber-like polymers, brittle and elastic-plastic polymeric foams, and biological tissues.

## 4.1 Challenges in Characterizing Soft Materials

Typical soft materials include elastomers, foams, gels, and soft biological tissues. These soft materials have common characteristics of low strength, stiffness, and wave impedance. The mechanical response of soft materials is sensitive to loading conditions such as the rate and state of loading. The low wave speeds in the soft specimens make stress equilibrium, a necessary condition for uniform deformation, much more difficult. The low strength makes the amplitude of the transmitted pulse too weak to be precisely measured. The sensitivities to strain rate and stress state make the requirement on the control over testing conditions much more strict.

The most challenging issue is to facilitate uniform deformation in a soft specimen when conducting Kolsky compression bar experiments because of the nature of low wave speeds in the soft specimens. In Kolsky-bar experiments, it is assumed that the specimen deforms uniformly so that the measurement of deformation averaging over the specimen length may represent any point-wise deformation. However, this assumption may not be satisfied automatically in soft material testing. Figure 4.1 shows the high-speed deformation images of an RTV630 rubber specimen (Song and Chen 2005). The specimen has the same diameter and thickness of 12.6 mm. The incident and transmission bars are at the right and left hand sides, respectively, in Fig. 4.1. The incident bar end moved in and then compressed the rubber specimen from the right side. At the very beginning of the loading ($t = 49.5$ μs), only the portion of specimen in contact with the incident bar was compressed as indicated in Fig. 4.1. With increasing time, the deformation propagates towards the other side,

W.W. Chen and B. Song, *Split Hopkinson (Kolsky) Bar: Design, Testing and Applications*, Mechanical Engineering Series, DOI 10.1007/978-1-4419-7982-7_4,

indicating stress wave propagation. At $t = 198.0\,\mu s$, the deformation of the rubber specimen at the transmission bar end becomes larger than that at the incident bar end. The specimen eventually achieves nearly uniform deformation ($t = 247.5\,\mu s$) due to the stress wave propagation back and forth in the specimen. In hence, the images in Fig. 4.1 clearly show that the rubber specimen does not deform uniformly over the most duration of loading.

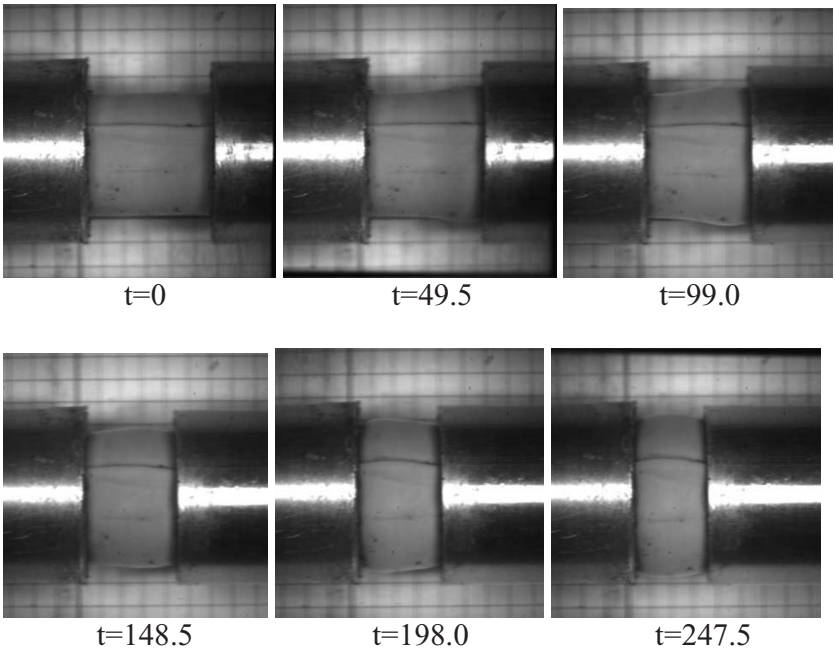


Figure 4.1 High speed deformation of an RTV630 rubber

Due to the characteristic of stress wave propagation in the specimen, the specimen will never achieve a state of ideal uniform deformation. However, the stress distribution can be considered uniform after several rounds of ringing up of stress waves inside the specimen. Ideally, this initial ringing-up process of stress wave inside the specimen should lead to stress equilibrium at the very early stages of dynamic loading.

The time for the elastic wave to propagate a single trip through the specimen is a critical parameter in the achievement of uniformity in stress distribution over the specimen length. Assuming the one-dimensional elastic wave speed in the specimen material is a constant, the time required for a single trip is

$$t_0 = \frac{l_0}{C_0} \tag{4.1}$$

where $l_0$ and $C_0$ are specimen length and elastic wave speed of the specimen material. The one-dimensional elastic wave speed is usually a characteristic constant for a certain material, making the specimen length as a critical variable to achieve uniform deformation. A thinner specimen clearly facilitates stress equilibrium sooner. A thin specimen also mitigates the possible stress wave attenuation in the specimen particularly when characterizing polymers possessing significant viscoelastic nature. However, a thin specimen makes the effect of interfacial friction between the specimen and bar ends more serious. In some cases, the entire specimen may not be under uniaxial stress loading at all, challenging appropriate data interpretation. The specimen length thus needs to be properly optimized while the interfaces between the specimen and bar ends are properly lubricated.

The non-uniform deformation in the axial direction also refers to axial inertia that produces stress and strain gradients along the axial direction. It is noted that, for some material like foams, the specimen deformation deviates from uniformity even though the stress may be consistent at both ends of the specimen because of their unique cell-collapse response. Figure 4.2 shows high-speed deformation process of an epoxy foam column with a 10×10 $mm^2$ cross section and a 19 mm length (Song and Chen 2005). It is observed that the failure (cell collapse) started from the incident bar end and then propagated to the other end (the transmission bar end). The propagation of such a failure front was defined as compaction wave, the speed of which is much slower than the elastic wave speed (Song et al. 2006c). The compaction wave divides the specimen into two different characteristic zones: compacted and uncompacted. The propagation of the compaction wave demonstrates the existence of drastic non-uniform deformation in the specimen, even though the stress in the specimen is globally uniform. The specimen stress during this process is represented with the plateau stress in the stress-strain curve (Fig. 4.3) (Song et al. 2006c). The unique deformation characteristic of the foam specimen makes it impossible to achieve uniform deformation under dynamic loading. However, in Kolsky-bar experiments on

soft materials, measures should be taken for the stress distribution in the specimen to be as uniform as possible.

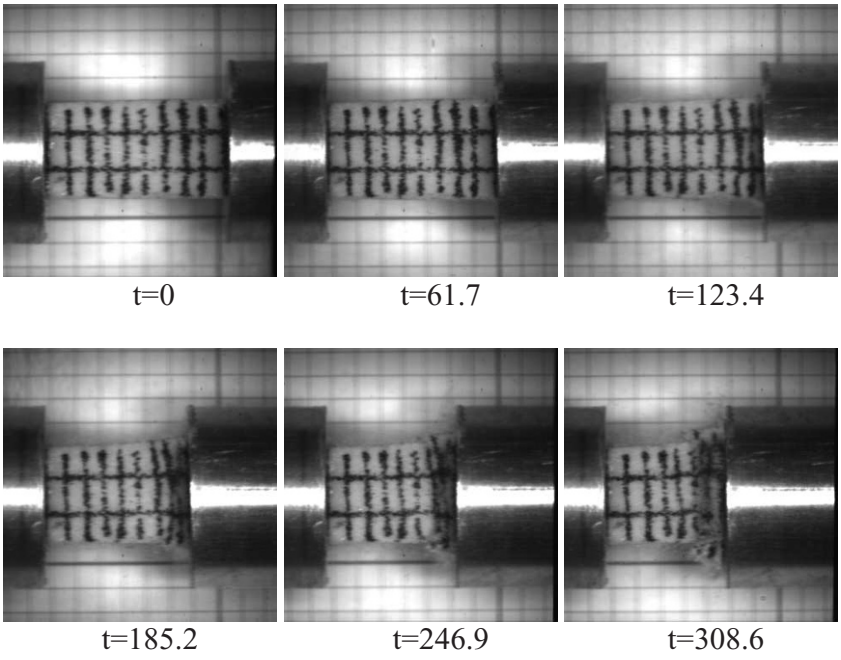


Figure 4.2 High speed deformation of an epoxy foam column

The non-uniform deformation presented in Figs. 4.1 and 4.2 is related to axial inertia encountered in dynamic loading. The axial inertia (or acceleration) also results in inertia along radial directions due to Poisson's effect. The radial inertia in turn produces extra axial stress on the specimen. The extra axial stress from radial inertia takes the form of a spike in the specimen stress measurement during the acceleration state of the dynamic deformation, as shown in Fig. 4.4 (Song et al. 2007e). The amplitude of this spike stress is in the order of 1 MPa, which could be neglected when characterizing many engineering materials. However, this amplitude is comparable to the strength of soft materials, and even higher than the strength of extra-soft materials. Since this spike is not

material intrinsic response, it should be removed from the stress measurement in dynamic characterization of soft materials, particularly extra-soft materials. The inertia-induced extra stress also takes a form of a downward spike during deceleration in axial direction.

As discussed in Chapter 2.3, the specimen aspect ratio (length-to-diameter ratio) determines the severity of both axial and radial inertia. An appropriate determination of specimen dimensions is required in the specimen design for Kolsky-bar experiments. This is applicable not only to the soft materials but also to all materials characterized with Kolsky bar since the inertia issue is independent of material strength. However, due to the low mechanical strength of soft materials, the inertia issue becomes much more severe that has to be taken care of in soft material characterization. The inertia in both axial and radial directions is related to the geometry and dimensions of the specimen and the acceleration the specimen experiences. Minimizing both axial and radial inertia in specimen can therefore be approached in both specimen design and loading-condition control.

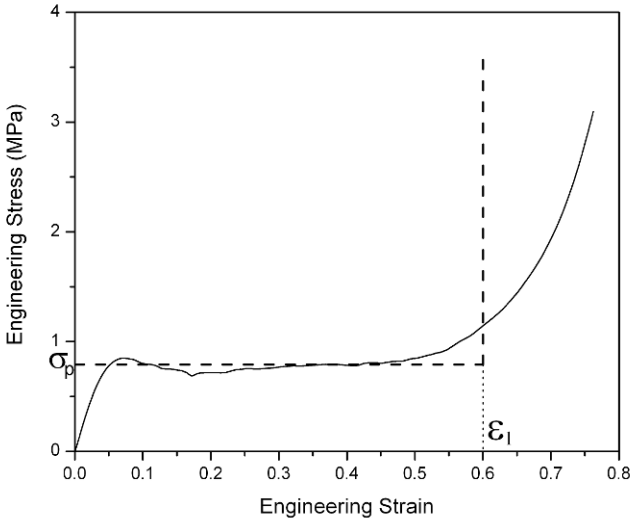


Figure 4.3 Typical stress-strain response of foam material
*(Reproduced from Song et al. (2006c) with permission)*

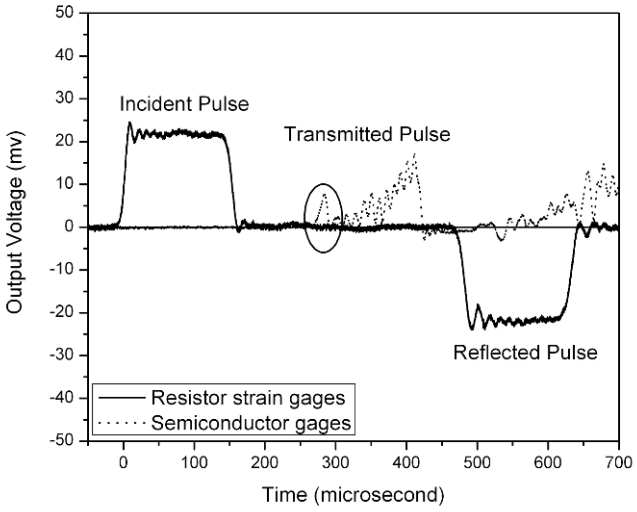


Figure 4.4 Stress spike in the transmitted pulse for soft material characterization *(Reproduced from Song et al. (2007e) with permission)*

The low strength of soft materials requires new techniques to detect the weak transmitted signals in Kolsky-bar experiments. Regular resistor strain gages are not sufficiently sensitive to measure the weak signals with a reasonable signal-to-noise ratio. Highly sensitive transducers are needed to record the weak signals transmitted through the soft specimen. The much lower wave impedance of the soft materials than the bar material makes a nearly full reflection of the incident pulse. Significant noise occurs when using (1.8) to calculate the stress at the incident bar/specimen end. This makes stress equilibrium verification nearly impossible. New techniques are needed to monitor the stress equilibration during dynamic loading.

Many soft materials are sensitive to strain rates. The strain rate in an experiment is not well defined if it varies during an experiment after the initial acceleration stage. Furthermore, the variation in strain rate also changes the stress-strain response for strain-rate-sensitive materials. Therefore, the strain rate is desired to be constant in a Kolsky-bar experiment. In a conventional Kolsky-bar experiment with a roughly con-

stant incident pulse amplitude, the strain rate that is proportional to the reflected pulse typically decreases as the deforming specimen transmits more and more load into the transmission bar. The profile of the incident pulse thus needs to be controlled to ensure constant strain-rate deformation in the specimen.

## 4.2 Specimen Design

As discussed in Chapter 2.3, to minimize both axial and radial inertia, both specimen length and diameter should be properly designed. When characterizing soft materials with Kolsky bar, the inertia becomes more severe due to the low strength of the soft materials.

Many soft materials are capable of large deformation under axial compression while large expansion along radial directions occurs. In a Kolsky-bar experiment, the specimen cross-sectional area (or diameter) should not exceed that of the bars. With the known bar diameter, the initial specimen diameter is limited for a desired axial compressive strain, or vice versa. For example, a specimen with an initial diameter of 12.7 mm loaded with 19-mm diameter bars will generate valid data up to an axial engineering strain of 55%. The assumption of incompressibility is usually used to approximate the little volume change in a specimen, i.e.,

$$\frac{\pi}{4} d_0^{\,2} l_0 = \frac{\pi}{4} d^2 l \tag{4.2}$$

where $d_0$ is the original specimen diameter and thickness, respectively; $d$ and $l$ are the current diameter and thickness, respectively, of the soft specimen during deformation; and in the case of compression experiments,

$$\frac{l}{l_0} = 1 - \varepsilon_E \tag{4.3}$$

where $\varepsilon_E$ is the engineering strain of the specimen (positive in compression). The maximum allowable specimen diameter during deformation is the bar diameter to ensure the rubber specimen stays within the bar end faces. The corresponding maximum original specimen diameter, $d_0$, for

a desired specimen strain, $\varepsilon_E$, and a given bar diameter, $d_{bar}$, can thus be calculated as

$$d_0 = d_{bar}\sqrt{1-\varepsilon_E} \tag{4.4}$$

For example, if the desired largest engineering strain is 0.7 when tested with 19.05-mm diameter bars, the corresponding maximum original diameter of the rubber specimen should be less than 10.43 mm.

Figure 4.5 shows the high-speed backlight images of an EPDM rubber specimen edge (~12.70-mm diameter, 1.60-mm thick) during dynamic compression (Song and Chen 2003). The apparent concave edge is actually the lubricant on the specimen/bar interfaces that is squeezed out by the laterally expanding specimen. When the engineering strain is larger than 0.6 ($t > 164.5\mu s$), the cross-sectional area of the rubber specimen exceeds that of the bars.

After the specimen diameter is determined, the specimen thickness could be optimized to minimize the inertia effects. However, when the Kolsky bar is employed to characterize soft materials, particularly extra soft materials, the general optimization of length-to-diameter ratio described in Chapter 2.3 may not be appropriate because of the low wave speed in the materials. Thinner specimen is desired to facilitate dynamic stress equilibrium.

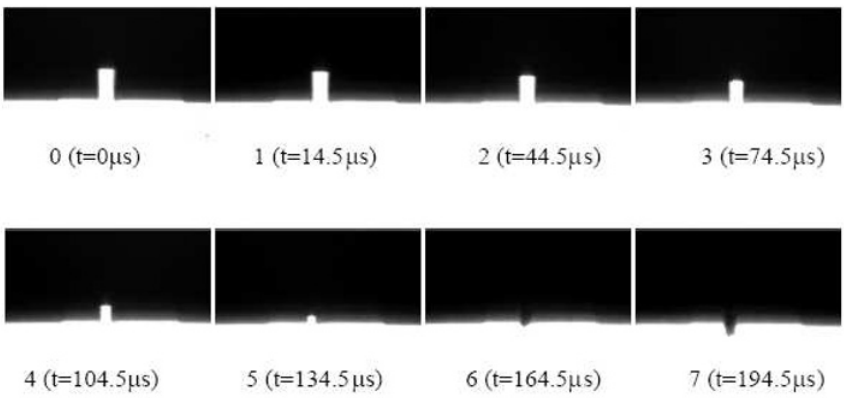


Figure 4.5 High-speed deformation of the EPDM rubber specimen
*(Reproduced from Song and Chen (2003) with permission)*

On the other hand, the thin specimen makes the interfacial friction between the specimen and the bar ends significant, necessitating sufficient lubrication. In the case of characterizing a foam specimen, a thin specimen may have few cell structures along the axial loading direction. The mechanical response obtained from such a thin specimen may thus be deviated from the actual response of the bulk foam. Therefore, in experiment design, trade-offs are made among the optimized length-to-diameter ratio, dynamic stress equilibrium, friction effects, and representative volume size.

Due to the nature of stress wave propagation, the stress equilibrium is not possible to be achieved perfectly in experiments. It is convenient to have an evaluation criterion for assessing stress equilibrium. One proposed criterion is that described in Chapter 3.5.3: the specimen is considered under uniform loading (dynamic stress equilibrium) when the ratio ($R(t)$) of stress difference ($\Delta\sigma(t)$) between both specimen ends to the mean value ($\sigma_m(t)$) within the specimen is less than 5%,

$$R(t)=\left|\frac{\Delta\sigma(t)}{\sigma_m(t)}\right|\le 0.05 \tag{4.5}$$

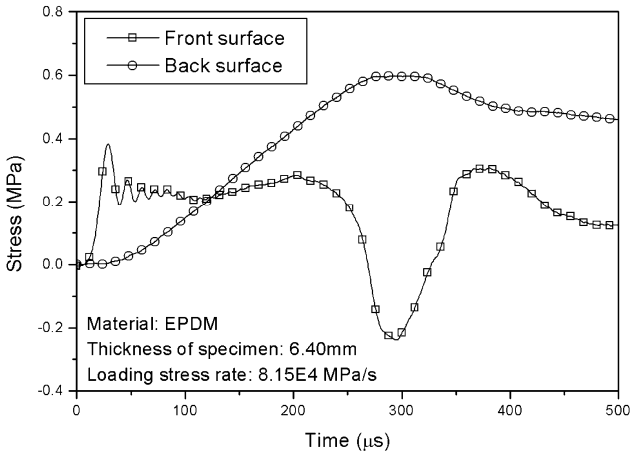


Figure 4.6 Comparison of stress at both ends of a 6.40-mm-thick EPDM rubber specimen
*(Reproduced from Song and Chen (2004b) with permission)*

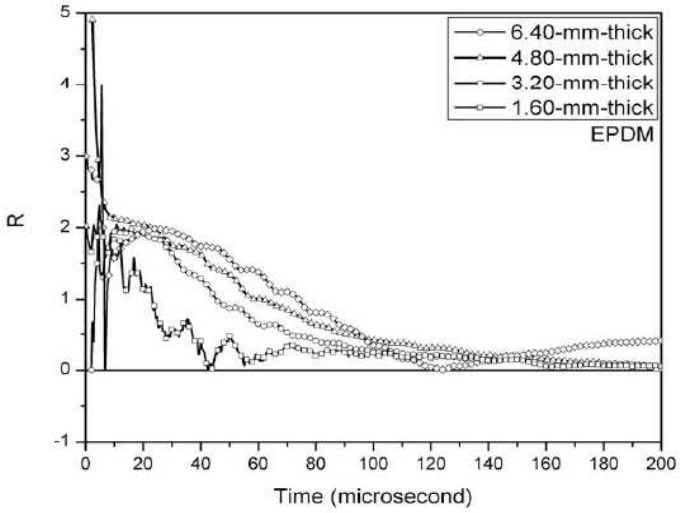


Figure 4.7 Effect of specimen thickness on dynamic stress equilibration

Once the stress equilibrium is defined, the optimized specimen thickness can be developed by judging the time to equilibrium. Figure 4.6 shows the stress histories at both ends of a 6.40-mm-thick EPDM rubber specimen loaded by a conventional Kolsky-bar incident pulse (Song and Chen 2004b). It is clearly shown that the specimen was far from stress equilibrium over the entire loading duration. The stress equilibration factor $R(t)$ is shown in Fig. 4.7 (Song and Chen 2005). Figure 4.7 also shows the comparison of the stress equilibration factor when the specimen thickness is reduced from 6.40 mm to 1.60 mm. The specimen becomes closer to stress equilibrium with reduced specimen thickness. Even though the specimen thickness is reduced to 1.60 mm, the stress in the specimen is still not in equilibrium. Therefore, a thin specimen is one of the requirements in Kolsky-bar experiments on soft materials but is not sufficient to achieve dynamic equilibrium. Further modifications, such as control of initial loading rate, are required. Lower rates of initial loading facilitate early stress equilibrium in the specimen. Constant strain-rate deformation minimizes the specimen inertia in Kolsky-bar experiments. Both initial loading rate and strain rate can be controlled with proper pulse shaping technique, as described in Chapter 2.5.

In addition to axial inertia, radial inertia in a soft specimen becomes significant at high rates of loading. When the specimen is subjected to dynamic axial compression, the axial acceleration also generates inertia (or acceleration) in the radial directions due to Poisson's effect, particularly when the specimen being characterized is nearly incompressible. This radial inertia, in turn, produces an extra axial stress in the specimen. This extra axial stress is not associated with the intrinsic mechanical properties of the material. As indicated in (2.8), the amplitude of the radial-inertia-induced axial stress depends on the specimen material density, the strain acceleration, and the specimen radius. In a typical Kolsky-bar experiment, this radial inertia-induced axial stress is in the order of 1-2 MPa. This amplitude is negligible for most engineering materials with two orders higher amplitude of strength. Therefore, specimen radial inertia issue is typically not mentioned in most Kolsky-bar experiments. However, for the soft materials with strength in the same or even lower order of amplitude, this radial-inertia-induced axial stress is no longer negligible. For example, the strength of brain tissues is only in the order of kPa, the extra stress of 1-2 MPa can easily overshadow the specimen's intrinsic mechanical response (Pervin and Chen 2009). Therefore, when testing soft materials in Kolsky-bar experiments, it is necessary to minimize the inertia effects through proper design of the experiments.

For an incompressible material under small elastic deformation, the extra stress caused by radial inertia is determined by closed-form solution,

$$\sigma_z = \sigma_\theta = \sigma_r = \frac{\rho_0 (a^2 - r^2)}{4} \varepsilon \tag{2.7}$$

The distribution of this extra stress $\sigma_z$ in the radial directions of the cylindrical (or disk) specimen is illustrated with solid line in Fig. 4.8 (Song et al. 2007e). The specimen has a radius of 5 mm. The distribution shows that the amplitude of the inertia-induced axial stress reaches the maximum at the specimen center but vanishes at the specimen edge. The averaged extra axial stress over the specimen cross section has been found consistent with Kolsky's original energy-based analysis (2.6). According to (2.6), if the strain rate is constant, the inertial term vanishes when the specimen deformation is small. However, it takes time for the strain rate to accelerate from zero to a desired constant level. The acceleration-induced inertia is inevitable during the initial stages of loading, even though the inertia may be reduced through the control over the initial acceleration. A reduced initial acceleration is also desirable for the soft

specimen to achieve stress equilibrium. A loading pulse with an extended rise time is commonly used to satisfy these experimental requirements.

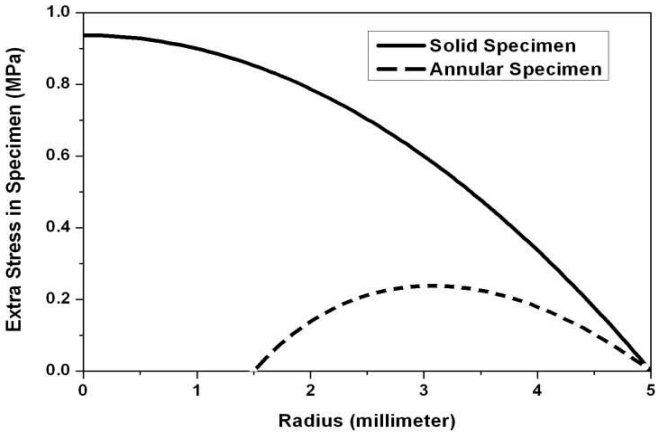


Figure 4.8 Extra axial stress distribution along radial direction in solid and annular specimens
*(Reproduced from Song et al. (2007e) with permission)*

Since the maximum stress induced by radial inertia incurs its maximum at the center of specimen (Fig. 4.8), an effective approach to minimize the inertia effects is to use a hollow specimen for Kolsky-bar characterization. An analysis has shown that the radial-inertia-induced stress can be significantly reduced when the central portion of the specimen is removed (Song et al. 2007e). The dashed line in Fig. 4.8 shows the distribution of the radial inertial stress induced axial stress along the radial direction of the specimen with a hole of 1.5 mm in radius cut at the center. As shown in Fig. 4.8, the extra stress is zero at both the inner and outer edges of the hollow specimen. The peak value of the inertia-induced stress is only 25% of that in a solid specimen. Parametric studies indicate that the radial inertia becomes insignificant when the inner diameter approaches to the outer diameter. However, in practical experi-

ments, when the initial acceleration is reduced, the 1.5-mm radius hole in a 5-mm radius specimen has been found to reduce the acceleration-induced extra stress to below experimental error level. Furthermore, with the quantitative analysis tool available, it is also feasible to numerically correct the acceleration-induced inertia effects when it is impractical to make hollow specimens or to reduce initial acceleration.

As indicated by (2.10), even after eliminating the acceleration induced extra stress, high strain rate itself can also produce inertia-induced stresses, especially when the strain in the specimen is large. For instance, when the engineering strain in the specimen approaches 1, the inertia-induced stress can overshadow the mechanical response in the specimen. Therefore, one needs to be cautious when interpreting experimental results from Kolsky bar experiments on a soft material deforming to large strains at high rates.

In summary, when the Kolsky bar is used to characterize soft materials, both specimen geometry and dimensions should be carefully designed to reduce the effects of both axial and radial inertia. In addition, the specimen should be under dynamic equilibrium and the strain rate needs to be constant. Before the strain rate reaches constant, the acceleration process in strain rate should be extended such that the inertia effects are minimized and the equilibrium is able to be achieved. When the soft specimen deforms to large strains at high rates, the data need to be carefully examined since a significant portion of the transmitted signal may come from inertia effects, even though the strain rates are maintained at constant levels after initial acceleration.

## 4.3 Pulse Shaping

In Kolsky-bar experiments, besides the design of specimen geometry, the profile of the incident pulse is the only controllable parameter to subject the specimen to desired testing conditions. The shape of the incident pulse is controlled through pulse shaping techniques. During the initial stages of the dynamic loading on a soft specimen, the incident pulse should have a relatively low rate of loading to achieve stress equilibrium in the specimen and to minimize acceleration-induced inertia. The continuing portion that follows the initial loading is properly modified according to the specimen response to facilitate constant strain rate deformation.

Compared to that in conventional Kolsky bar experiments, the rise time of the incident pulse should be significantly increased through pulse shaping. For example, at least 100 microsecond rise time, nearly an order of magnitude longer than that in conventional Kolsky-bar experiments, of the incident pulse is required for stress equilibrium in a rubber specimen (Song and Chen 2004b). After the initial rising, the profile of the incident pulse is altered to maintain a constant strain rate deformation in the specimen, as indicated by a reflected pulse with a plateau according to (1.12). Under stress equilibrium, the incident pulse is the sum of reflected pulse and transmitted pulse. The transmitted pulse is proportional to the stress history in the specimen under investigation. The desirable profile of the incident pulse is the transmitted pulse plus a constant reflected pulse. Different constant levels of the reflected pulse represent different constant strain rates in the soft specimen. When the transmitted pulse is comparable to the reflected pulse, the incident pulse is desired to have a similar profile but with higher amplitude in comparison to the transmitted pulse, as illustrated in Fig. 4.9. However, when the specimen material is very soft, the amplitude of the transmitted pulse may be negligible as compared to the reflected pulse. In this case, the desired incident pulse is a plateau with a long rise time prior to the plateau, which is illustrated in Fig. 4.10. Since the profile of the transmitted pulse of a soft specimen is not known under a specific set of testing conditions, the generation of a proper incident pulse profile is iterative in nature.

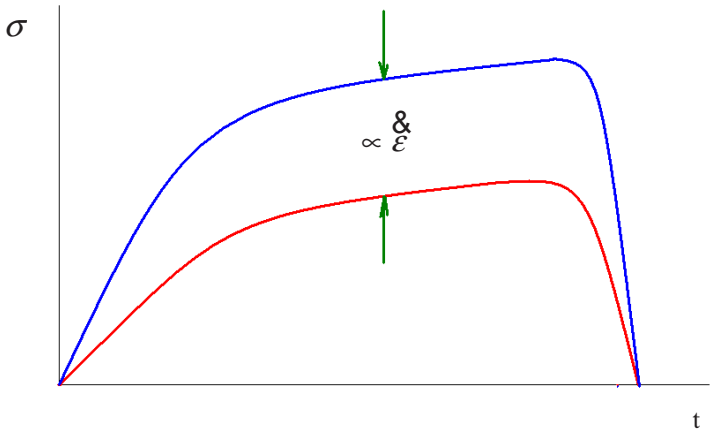


Figure 4.9 Illustration of incident pulse design for soft materials

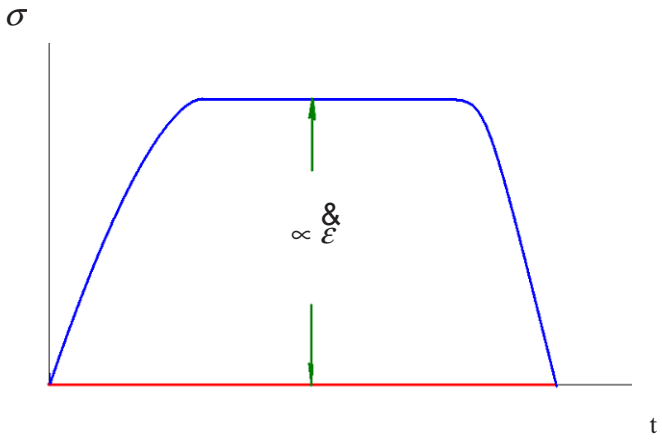


Figure 4.10 Illustration of incident pulse design for extra-soft materials

In order to generate the desired incident pulse, pulse shapers are generally employed. However, the selection of pulse shaper is quite diversified for different soft materials. In addition to the copper pulse shaper that has been analytically modeled, paper, copper tubes, and even foam disks are also commonly used as pulse shapers for soft material characterization. In Chapter 4.5, we will give examples for soft material characterization including pulse shaping techniques.

## 4.4 Force Sensing

Force sensing becomes more challenging in Kolsky-bar characterization of soft materials, such as biological tissues, which possess strengths in the order of kPa. In Kolsky-bar experiments, the specimen stress is calculated from the amplitude of transmitted pulse (1.14). The high stiffness of the bar material is desired to maintain a high wave impedance mismatch between the specimen and the bars for early dynamic equilibrium. In such a system, each reflection of the stress wave at the specimen/bar interface nearly doubles the stress amplitude in the specimen. It is desir-

able to build up the stress amplitude as much as possible from each reflection in the soft specimen quickly since the number of stress wave reflections is limited during an experiment due to the low wave speed. However, the low stress in the specimen produces extremely low strain in the stiff transmission bar. For instance, the stress of 1 MPa in the specimen with 10 mm in diameter transits into 0.25 MPa in a 20-mm-diameter transmission bar. This 0.25 MPa stress produces only 1.25 microstrain in a steel transmission bar. It is very difficult to clearly detect such a small strain by regular strain gages mounted on the steel bar surface. The force sensing components in conventional Kolsky-bar systems need to be improved to obtain a high signal-to-noise measurement in specimen stress.

According to (1.14), under a constant stress level on the left side of the equation, there are two approaches to increase the amplitude of the transmitted strain signal, $\varepsilon_T$. One is to reduce the bar material stiffness, $E$; and the other is to reduce the bar cross-sectional area, $A_B$. To examine the possibilities in bar material selection, Table 1 lists the modulus of elasticity, density, and mechanical impedance ( $\rho C$ or $\sqrt{\rho E}$ ) for different metallic and polymeric materials in comparison to steel that is used in conventional Kolsky bars. It is shown that the aluminum alloy has a modulus of approximately one-third of steel, which means that the strain signal will be amplified by three times in amplitude for a certain transmitted stress if using aluminum as the bar material. In fact, the aluminum alloy has been very popularly used as the bar material in Kolsky-bar experiments on soft polymers and polymeric foams (Chen et al. 2002b). Other metallic materials including titanium and magnesium have also been recommended as the bar material for soft material characterization (Gray et al. 1997, Gray and Blumenthal 2000, Shergold et al. 2006). These materials have even much lower Young's moduli than aluminum, and are capable of sensing weaker transmitted signals. However, the relatively low yield strengths limit their application to materials characterization.

Table 4.1 Mechanical Parameters of Various Materials

| Material | Density, $\rho$, ($kg/m^3$) | Elastic Wave Speed, $C$, (m/s) | Young's Modulus, $E$, (GPa) | Wave Impedance, $\rho C$ or $\sqrt{\rho E}$, ($kg/m^2/s$) |
|---|---|---|---|---|
| C350 Maraging Steel | 8000 | 5000 | 200 | $4\times10^7$ |
| 7075-T6 Aluminum | 2810 | 5051 | 71.7 | $1.42\times10^7$ |
| CA-1000-1 PMMA | 1160 | 1313 | 2.0 | $1.52\times10^6$ |
| Rubber | 930 | 46 | 0.002 | $4.28\times10^4$ |

Due to their much lower stiffness, polymeric materials have been used as bar materials for characterization of soft polymers and polymeric foams. Common polymers used as the bar materials include polymethyl methacrylate (PMMA), nylon, and polycarbonate (PC). The low Young's moduli of these materials yield higher sensitivities than the metallic materials. However, the gains in sensitivity are limited. One limitation is the heat conductivity of the polymeric materials. When a strain gage is mounted on the bar surface, heat is generated when the electric current passes through the gages. When the gages are on metallic bar surfaces, the heat is easily dissipated through the bars, leaving the strain gages at nearly the same temperature as the bars. Furthermore, the temperature is nearly constant after the warm-up of the data acquisition system. When the gages are on the polymer bar surfaces, the poor heat conductivity of the polymers leads to temperature rise in the gages. To avoid excessive temperature in the gages, the exitation voltage to the Wheatstone bridges is severely limited, typically lowered by an order of magnitude. As expressed by (1.42) or (1.48), at a given strain, the amplitude of the output signal is directly proportional to the excitation voltage. An excitation voltage of an order of magnitude lower offsets most of the potentials gained from the lower stiffness of the polymeric bars.

In addition to the limited excitation voltage, the nature of viscoelasticity of the polymeric bars further limits their utilization as the bar material in Kolsky-bar experiments. The viscoelasticity brings dispersion and attenuation of stress waves in propagation. Dispersion distorts the profile of a stress wave while attenuation decreases its amplitude. Therefore, the stress wave measured at the strain gage location is no longer representative of the stress wave at the interface between the specimen and bar ends. The stress wave signal measured at the strain gage location must be corrected back to the specimen/bar end interface. The typical viscoelastic response of the polymeric materials makes the relationship between the surface strain measurements and the axial stresses in the bars depend on strain rate, temperature, humidity, and aging. All these increase uncertainties in the mechanical response of the specimen material obtained using the polymeric bars. Therefore, the use of polymer bars is mostly limited to special situations where metallic bars are not applicable such as in microwave environments.

The other approach to increase the bar sensitivities but still using metallic bars is to use hollow bars. Bar sensitivity can be increased when the bar cross-sectional area is reduced, for example, by employing hollow tubes as bars. A common bar combination in soft material characterization is to use a solid aluminum bar as the incident bar and a hollow bar with the same material as the transmission bar. In this case, the hollow transmission bar works as a linear elastic stress/strain amplifier.

Since the axial stress in the tube is also related to the surface axial strain by the bar material's Young's modulus, no further complication is introduced by the incorporation of hollow transmission bars except for possible issues associated with elastic wave propagation in tubes. Since the incident and transmission bars are different in cross-sectional areas, the classic data reduction equations for calculation of strain rate and strain (Eqs. (1.12) and (1.13)) are no longer applicable, which need to be modified (Chen et al. 1999),

$$\varepsilon(t)=\frac{C_0}{l_0}\left(1-\frac{A_i}{A_t}\right)\varepsilon_I(t)-\frac{C_0}{l_0}\left(1+\frac{A_i}{A_t}\right)\varepsilon_R(t) \tag{4.6}$$

$$\varepsilon(t)=\frac{C_0}{l_0}\left(1-\frac{A_i}{A_t}\right)\int_0^t\varepsilon_I(\tau)d\tau-\frac{C_0}{l_0}\left(1+\frac{A_i}{A_t}\right)\int_0^t\varepsilon_R(\tau)d\tau \tag{4.7}$$

where $A_i$ and $A_t$ are cross-sectional areas of the solid incident and the hollow transmission bars, respectively. Unlike Eq. (1.12), the strain rate is not proportional to the amplitude of reflected pulse when the hollow transmission bar is used. This may bring difficulties in experimental design to obtain constant strain rate in the specimen. Equations (4.6) and (4.7) yield to Eqs. (1.12) and (1.13), respectively, when the transmission bar has the same diameter and material as well, as the incident bar.

Besides working with the bar material and cross-sectional area to increase the amplitude of the transmitted pulses, another direct solution is to utilize highly sensitive transducers. The commonly used resistor strain gage on the bar surface has a gage factor of approximately 2.0. However, the semiconductor strain gage factor is approximately 150. The over 70 times higher sensitivity of the semiconductor strain gage is able to satisfy the measurement requirement for most soft materials. A combination of semi-conductor strain gages and hollow bars satisfies most needs in transmitted signal sensing except for some extreme cases. Another approach to precise force measurements is direct force (or stress) measurement using highly sensitive force transducers. X-cut circular piezoelectric quartz crystal force transducers have been applied to Kolsky-bar experiments on soft materials. These force transducers have been used to measure dynamic force profiles for many years. The 0.254±0.025 mm thick quartz crystal force transducer used by Chen et al. (2000) has a piezoelectric constant of 2.30 pC/N. The quartz crystal has an excellent linearity up to the pressure where dielectric breakdown occurs and is not very sensitive to environmental temperatures. The quartz crystal also has a mechanical impedance ($\rho C_o$) of approximately

$1.394\times10^7$ kg/m$^2$s, which is very close to the impedance ($1.350\times10^7$ kg/m$^2$s) of aluminum alloy. Therefore, when the quartz crystal force transducers are embedded into aluminum bars, the disturbance to the one-dimensional stress wave propagation in the bar system is minimal.

The quartz crystal force transducer is able to directly measure the force (or stress) of the specimen not only on the transmission bar side but also on the incident bar side. When the specimen material is soft, it is difficult to measure the force (or stress) at the front side of specimen to verify the force (or stress) equilibration process because the amplitudes of the incident and reflected pulse are very close. The difference between the two large-amplitude pulses is noisy and hard to be compared to the low-amplitude transmitted signal. When the quartz crystal is attached to the interface between the incident bar and the specimen, the force at this interface can be measured directly instead of taking the difference between the incident and reflected signals.

The quartz crystal force transducer is glued with conductive epoxy on the bar end. In order to protect the quartz crystal force transducer, a thin aluminum disc is usually glued on the other side of quartz crystal. However, the thin aluminum disc may bring additional axial inertia force, particularly when it is subjected to significant acceleration generated by the high-amplitude incident pulse. This axial inertia force makes the measurement from the quartz crystal force transducer different from the actual force history on the specimen (Casem et al. 2005),

$$F_{1m} = F_1 + m_e a_1 = F_1 + m_e C_0 \frac{d\left(\varepsilon_i - \varepsilon_r\right)}{dt} \tag{4.8}$$

$$F_{2m} = F_2 - m_e a_2 = F_2 - m_e C_0 \frac{d\varepsilon_t}{dt} \tag{4.9}$$

where $F_{1m}$ and $F_{2m}$ are forces directly measured by the quart crystal force transducers at the front and back ends of the specimen, respectively; $m_e$ is the effective mass that carries the additional axial acceleration,

$$m_e = \frac{1}{2} m_g + m_1 \tag{4.10}$$

In (4.10), $m_g$ and $m_1$ are masses of the quartz crystal transducer and the aluminum disc; respectively. The last terms in both (4.8) and (4.9) represent the additional axial inertia forces brought by the additional alumi-

num discs and the quartz crystals themselves at both ends of the specimen. When testing soft materials, the transmitted signal is so weak that the acceleration at the specimen back end can be neglected. However, at the front end of the specimen, the acceleration is too significant to be negligible. Note that the incident and reflected strains have opposite signs.

This axial inertia force at the front end needs to be corrected or compensated. A numerical correction can be performed according to (4.8) after measurement of the masses of the quartz crystal and the aluminum disc as well as both incident and reflected pulses. Alternatively, a so-called "three-quartz technique" has been developed to experimentally compensate the axial inertia force, which is illustrated in Fig. 4.11 (Casem et al. 2005). When $m_s$ and $m_p$ satisfy the following relationship,

$$m_s = m_p - \frac{1}{2} m_g \tag{4.11}$$

the additional inertia force is automatically compensated. Figure 4.12 shows the comparison of Kolsky-bar experiments on a polymeric foam with the single quartz crystal and the "three-quartz crystal" technique (Casem et al. 2005). The records clearly show that, without the compensation of the additional axial force, the stress equilibration could be assessed at fault. Since the inertia is related to acceleration, the axial inertia force vanishes under constant-speed loading. In Kolsky-bar experiments, the initial acceleration is of high amplitude and inevitable. In hence, the axial inertia force brought by introducing the quartz crystal and attached aluminum disc should be corrected or compensated when testing soft materials.

Another possible transducer for direct force sensing is polyvinylidene fluoride (PVDF). This thin-film type of force transducer has approximately one order of magnitude higher sensitivity than the quartz crystal force transducers. However, the possible nonlinearity of the sensitivity of the PVDF requires accurate calibration within the full range of application, which is not yet available (Ueberschlag 2001).

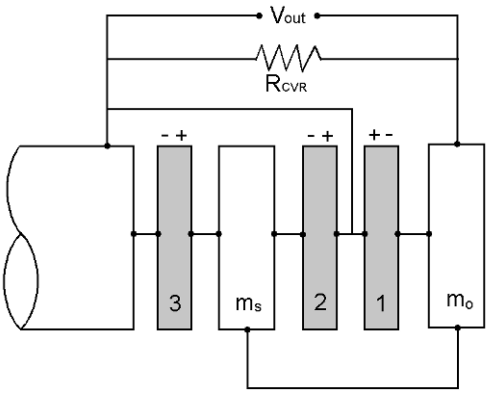


Figure 4.11 Three-quartz technique
*(Reproduced from Casem et al. (2005) with permission)*

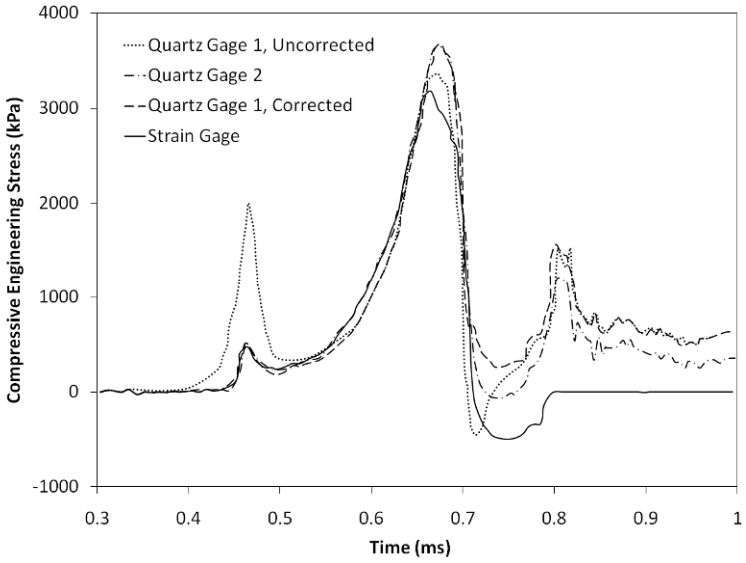


Figure 4.12 Comparison of single-quartz and three-quartz techniques
*(Reproduced from Casem et al. (2005) with permission)*

## 4.5 Experiment Design

As described in previous sections, considerations for valid Kolsky-bar experiments should be focused on specimen design, force sensing, and pulse shaping design with the goal of achieving uniform deformation/stress equilibration and constant strain rate deformation in the specimen.

Due to different mechanical responses of different soft materials to high-rate loading, the detailed experiment designs for these materials are diversified. Figure 4.13 illustrates a general layout of the Kolsky-bar setup modified for soft material characterization. The bars are usually solid rods being made of low-stiffness alloys such as aluminum alloy. In the cases where the transmitted signal is too weak, the transmission bar is hollow, and/or with highly sensitive strain gages, such as semiconductor strain gages. As compared to the conventional setup in Fig. 1.6, the Kolsky bar is modified with the employment of the pulse shaper that is placed on the impact end of the incident bar, and quartz-crystal force transducers that are attached to the specimen ends of the incident and transmission bars, respectively. Again, the transmission bar may be hollow. In addition, to preserve the deformed state in the specimen after high-rate loading, the incident bar can be modified to single-loading type, as described in Chapter 2.6, to ensure single loading on the soft specimen.

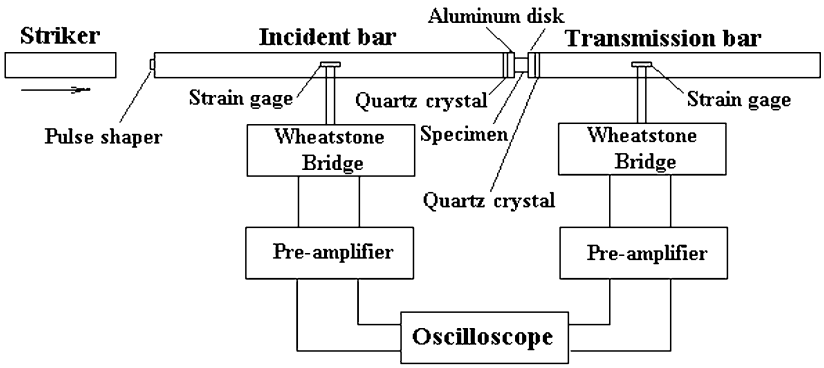


Figure 4.13 Kolsky-bar setup for soft material characterization

Most soft materials can deform to large strains, the bars thus need to be sufficient long to enable the needed long duration of loading to the specimen. When long bars are used, stress wave dispersion, as described in Chapter 2.1, during propagation may become significant due to two-dimensional effect (Poisson's effect) of the bars. One purpose of the pulse shaping is to efficiently minimize the stress wave dispersion as a physical low-pass filter that eliminates dispersive high-frequency wave components. The pulse shaper also needs to be properly designed to produce a desired profile of the incident pulse facilitating stress equilibration and constant strain-rate deformation in the specimen, depending on the mechanical response of the specimen material.

The quartz-crystal force transducers are used to monitor the process of stress equilibrium in specimen during high-rate loading. Since the existence of quartz-crystal transducers should not influence the stress wave propagation, the quartz-crystal force transducers are ideally very thin circular discs with the same diameter as the bars. The mechanical impedance of the quartz-crystal force transducers should be as close as the bar material, which limits the material to be aluminum alloys. The axial inertia brought by the additional disc at the incident bar end needs to be compensated numerically or by using three-quartz technique. Such a compensation of axial inertia on the transmission bar side is usually not necessary due to the low transmitted pulses through the soft specimens.

Even though the specimen dimensions and geometry may vary from material to material, the soft specimen always needs to be thin as a general principle for specimen design. Such a thin specimen may increase the influence of interfacial friction between the soft specimen and the bar ends. Significant interfacial friction makes the specimen in multiaxial stress state, which will erroneously increase the strength of the specimen material. A barrel shape of the specimen during high-rate deformation is a typical indicator of insufficient interfacial lubrication. The effect of lubrication on specimen response in Kolsky-bar experiments has been investigated (Briscoe and Nosker 1984, Zenker and Clos 1998, Trautmann et al. 2005). Petroleum jelly has been recognized as a good lubricate for most soft materials (Trautmann et al. 2005). However, for some special materials, e.g., biological tissues, the petroleum jelly is too viscous to provide sufficient lubrication for such extra-soft materials. Vegetable oils have been successfully used for biological tissues and gelatins in Kolsky-bar experiments (Moy et al. 2006, Song et al. 2007b, Pervin and Chen 2009).

In the following sections, we give several examples of Kolsky-bar experiment designs for different soft materials, which may be used for references when characterizing different materials but with similar characteristics.

### 4.5.1 Polymethyl Methacrylate (PMMA)

The PMMA specimens were machined into cylinders with a diameter of 12.70 mm and a thickness of 6.35 mm, making a length-to-diameter ratio of 0.5, from a commercially available rod. In order to relieve the residual stress in the specimens due to material handling and machining, all PMMA specimens were heat-treated in a sealed furnace to 110˚C for 4 hours, and then cooled down to room temperature overnight.

7075-T651 aluminum alloy was selected as the bar material. The bars had a common diameter of 19.05 mm. Since the yield strength of the PMMA is a significant fraction of that of the bar material, the transmitted signal could be easily detected with regular resistor strain gages mounted on the solid aluminum transmission bar. In addition, the quartz-crystal force transducers in Fig. 4.13 are not necessary because the stresses at both ends of the specimen can be calculated with (1.8) and (1.9) without ambiguity for stress equilibrium evaluation. The specimen ends were lubricated with petroleum jelly.

As a typical viscoelatic material, both loading and unloading response of the PMMA are of interest. However, the experimental conditions, such as strain rate, during loading and unloading should be maintained the same to obtain the dynamic hysteretic response of the material. In this case, a special pulse shaping design is required because not only the loading profile but also the unloading profile of the incident pulse is in need of precise control to subject the specimen to desired testing condition during the experiment.

A pulse shaping technique, shown in Fig. 2.22, has been used for the PMMA characterization. The front pulse shaper is used to generate a desired incident loading profile for stress equilibrium and constant strain rate over the loading phase of the experiment. The rear pulse shapers on the surface of the rigid mass start to play the role, after the gap between the flange and the rigid mass is closed, to modify the unloading path of the incident pulse appropriately for stress equilibrium and the same constant strain rate over the unloading phase of the experiment.

In this case, a 3.97-mm-diameter, 1.57-mm-thick C11000 half-hardened copper disk was employed as the front pulse-shaper and two 2.38-mm-diameter, 0.51-mm-thick annealed C11000 copper disks were selected as the rear pulse-shapers. The gap between the flange and the rigid mass was preset at 0.89 mm. The incident pulse generated through such a special pulse shaping technique, and consequent reflected, and transmitted pulses for the PMMA at a strain rate of 360 $s^{-1}$ are shown in

Fig. 4.14 (Song and Chen 2004c). Figure 4.14 also shows that both dynamic stress equilibrium and constant strain rates were achieved in both loading and unloading portions. In addition, the unloading strain rate is maintained to be the same as the loading strain rate. The same strain rate for loading and unloading makes the resultant stress-strain loop at a common constant strain rate for strain-rate-effect investigation.

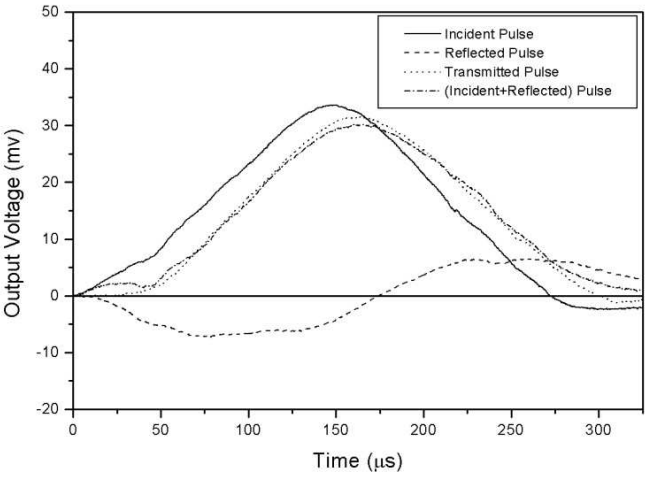


Figure 4.14 Kolsky-bar experiment on PMMA
*(Reproduced from Song and Chen (2004c) with permission)*

Figure 4.15 shows the stress-strain loops at one dynamic strain rate of 360 $s^{-1}$ and two quasi-static strain rates of 0.0001 $s^{-1}$ and 0.01 $s^{-1}$ (Song and Chen 2004c). All stress-strain curves exhibit similar characteristics: a nearly linear behavior at small strains (<3%) followed by a non-linear behavior in both loading and unloading portions. The unloading stress is lower than that of loading at a certain strain, making the stress-strain loop with a residual strain, or permanent set. The non-linear behavior and the residual strains after mechanical tests may indicate the presence of damage to the microstructures of the materials. Moreover, the residual

strain was found to depend on the maximum loading strain in the specimen: a larger maximum loading strain leads to a larger residual strain. Figure 4.15 also shows that the stress-strain loops are significantly sensitive to strain rate. The strong rate-sensitive hysteretic stress-strain loops verify the viscoelastic nature of the material.

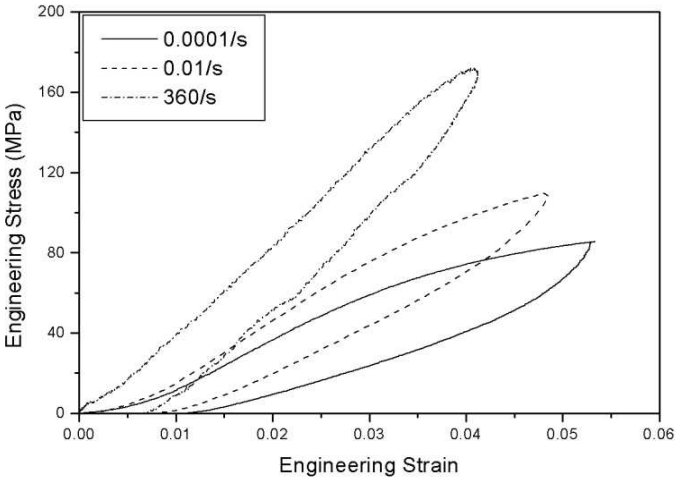


Figure 4.15 Loading and unloading stress-strain curves of PMMA
*(Reproduced from Song and Chen (2004c) with permission)*

## 4.5.2 Rubbers

Rubbers typically exhibit characteristics of nonlinear large deformation and significant sensitivity to strain rate and stress state. The low stress wave speed makes it challenging to achieve uniform deformation and stress equilibrium under high-rate loading, as shown in Fig. 4.1. The

rubber specimen needs to be thin and requires a low-rate initial loading to achieve stress equilibrium. As a role of thumb, a 3-mm-thick specimen is perhaps appropriate for achieving stress equilibrium after proper pulse shaping technique is used to produce low rate in the initial loading (or relatively long rise time in the incident pulse). The incident pulse has a rise time of as long as 100 μs which is approximately 10 times longer than that in conventional Kolsky-bar experiments. Petroleum jelly has also been found to provide sufficient lubrication for rubber testing.

### 4.5.2.1 Soybean-Oil Based Polymers

In this section, we present Kolsky compression bar experiments on soybean-oil based polymers, which have similar characteristics as other engineered rubbers. The materials are polymers made through the reaction of epoxidized soybean oil (ESO) with diamine compounds. The ESO was mixed thoroughly with the curing agent, triethylenetetramine (TETA) or diethylenetriamine (DETA), with different fractional amounts, as tabulated in Table 4.2 (Song et al. 2006b).

Table 4.2 Composition of soybean-oil based polymers
*(Reproduced from Song et al. (2006b) with permission)*

| Sample code | ESO (g)[a] | Curing agent (g)[a] | | | $T_g$ (°C) |
|---|---|---|---|---|---|
| | | TETA | DETA | TETA | |
| ESOT-I | 140.6 (0.141) | 40.3 (0.28) | | | 7.84 |
| ESOD | 149.1 (0.149) | | 30.3 (0.29) | | 1.51 |
| ESOT-II | 152.3 (0.152) | | | 27.5 (0.19) | 0.22 |

[a] Values in parentheses indicate moles.

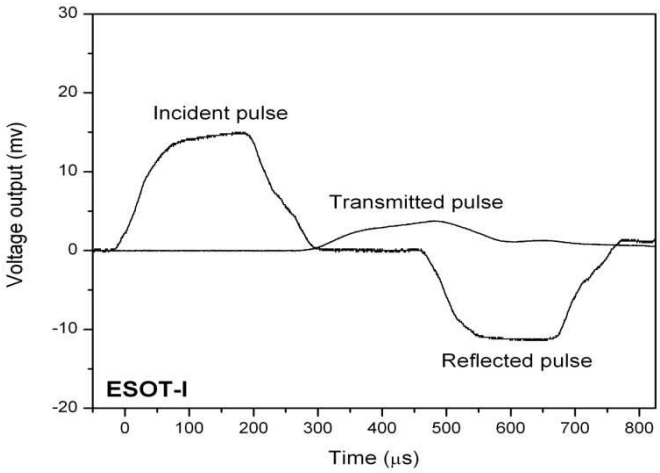


Figure 4.16 Kolsky bar experiment on ESOT-I
*(Reproduced from Song et al. (2006b) with permission)*

Figure 4.16 shows typical incident, reflected, and transmitted pulses in a Kolsky-bar experiment on the ESOT-I polymer listed in Table 4.2 (Song et al. 2006b). An annealed C11000 copper disk was employed as the pulse shaper in the experiment. The incident pulse had a rise time of about 100 μs. This long rise time during the initial portion of the incident pulse was generated for achieving stress equilibrium in the specimen. The dynamic stress equilibrium process in the ESOT-I rubber, which was monitored by the quartz transducers, is shown in Fig. 4.17. Figure 4.17 clearly indicates that the specimen was in dynamic stress equilibrium over the entire loading duration. As shown in the transmitted pulse, the stress in the specimen continuously increases under continuous compression. This type of specimen response requires more input energy to maintain constant strain rate in the specimen. Accordingly, the amplitude of incident pulse needs to be increased with time for this purpose. The increase rate for the amplitude of this incident stress needs to be carefully designed. If the rate is not sufficiently high, the strain rate in the specimen will still decrease even though the decrease rate may be slowed down by the pulse shaping. On the other side, if the incident stress is over supplied, the specimen will be compressed in acceleration. In this

set of experiments, the nearly linear portion in the incident pulse was generated for constant strain rate deformation in the specimen, which is shown in Fig. 4.16. However, the strain rate was not achieved to a constant until 100 μs after initial loading due to the long rise time in the incident pulse and the resultant strain rate acceleration from zero to the desired level. Strictly, the data obtained during the first 100 μs are not accurate, even though the stress may have been equilibrated by the end of this stage, because the strain rate has not achieved a constant yet. It is noted that the deformation produced in the first 100 μs may not be large due to the low strain rate before achieving the constant value. However, the accumulated strain in the specimen during the first 100 μs serves as a dividing point on the stress-strain curve that separates the valid and invalid portions of the dynamic stress-strain curve.

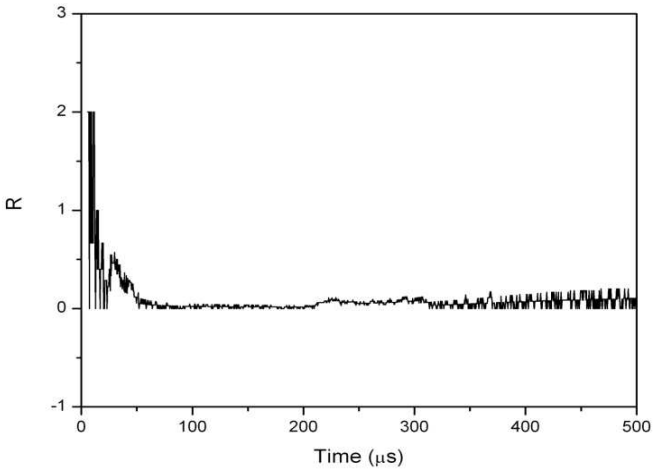


Figure 4.17 Dynamic stress equilibrium in the ESOT-I specimen
*(Reproduced from Song et al. (2006b) with permission)*

Figure 4.18 shows the engineering stress-strain curves for the ESOT-I at various dynamic strain rates from 230 to 1650 $s^{-1}$ (Song et al. 2006b). In order to study the strain-rate effect over a wide range, quasi-static stress-strain curves are also plotted in the same figure. Following the same procedure, the stress-strain curves for the other two materials

(ESOD and ESOT-II) listed in Table 4.2 are obtained and shown in Figs. 4.19 and 4.20, respectively. Significant strain-rate effects were found on all three materials, which also exhibit similar shapes in stress-strain curves. Not only stress amplitudes at certain strains but also the shapes of the stress–strain curves change due to strain rate effects when comparing the dynamic stress-strain curves to their quasi-static counterparts. An initial nearly linear behavior followed by a transitional nonlinear response and then a strain-hardening behavior is typical characteristic for the dynamic stress–strain curves. However, the initial linear behavior in quasi-static stress–strain curves is not significant when strain rate is below 1.0 $s^{-1}$. The tangential moduli in the quasi-static stress–strain curves increase with increasing strains.

The unloading part for the stress-strain curve of ESOT-I at 1650 $s^{-1}$ is plotted in Fig. 4.18. This is a typical unloading curve obtained from Kolsky-bar experiments on rubber or rubber-like materials. However, this measured unloading response may not represent the actual unloading process in the specimen material. When the specimen is unloaded, the viscoelastic nature makes it recover but with very low stress amplitude. This small stress produced by the specimen recovery may not be sufficiently high to push the compression bars back so that the specimen keeps being deformed but the stress is relaxed due to the nature of viscoelasticity.

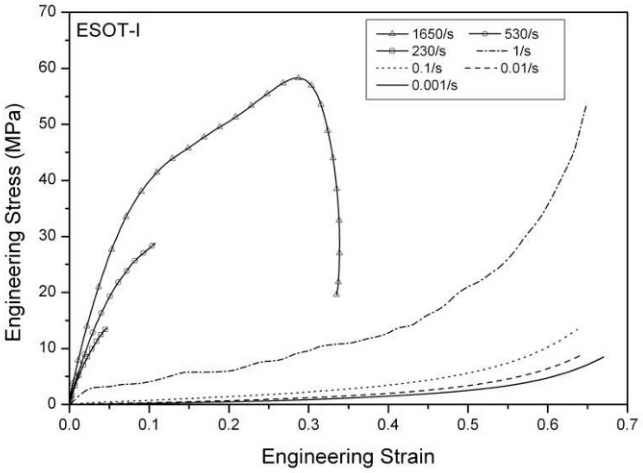


Figure 4.18 Compressive stress-strain curves of ESOT-I
*(Reproduced from Song et al. (2006b) with permission)*

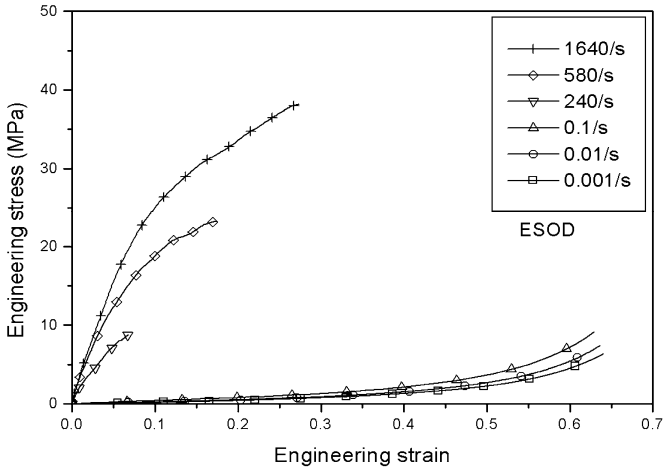


Figure 4.19 Compressive stress-strain curves of ESOD
*(Reproduced from Song et al. (2006b) with permission)*

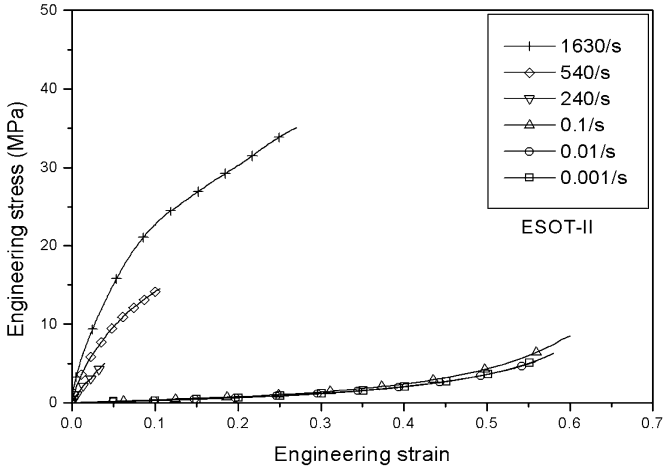


Figure 4.20 Compressive stress-strain curves of ESOT-II
*(Reproduced from Song et al. (2006b) with permission)*

### 4.5.2.2 ESO-NanoClay Composites

The composites with the ESO polymers as matrix and nanoclay (Closite 30B particles: montmorillonite modified with alkyl quaternary ammonium montmorillonite) as fillers exhibit very similar mechanical response as the base ESO polymers. However, the stresses at certain strains may either increase or decrease in comparison with the matrix material, depending on the weight of nanoclay and strain rate. The stress-strain curves of the three materials with 0, 5%, and 8% nanoclay in weight, respectively, were obtained using the same procedure for the ESO copolymer characterization and are shown in Figs. 4.21, 4.22, and 4.23, respectively (Song et al. 2006a).

The effects of strain rate and nanoclay-weight are summarized in Table 4.3. Consistent strain-rate hardening was observed for the composite with 5% nanoclay in weight. However, for the composite with 8% nanoclay in weight, the stress at the strain of 5% at the strain-rate of 2540 $s^{-1}$ is slightly lower than that at the same strain but at a lower strain rate of 700 $s^{-1}$ (Table 4.3). The disappearance of strain-rate hardening at this nanoclay weight may be caused by interface decohesion between the nanoclay and the ESO material due to too high load of nanoclay.

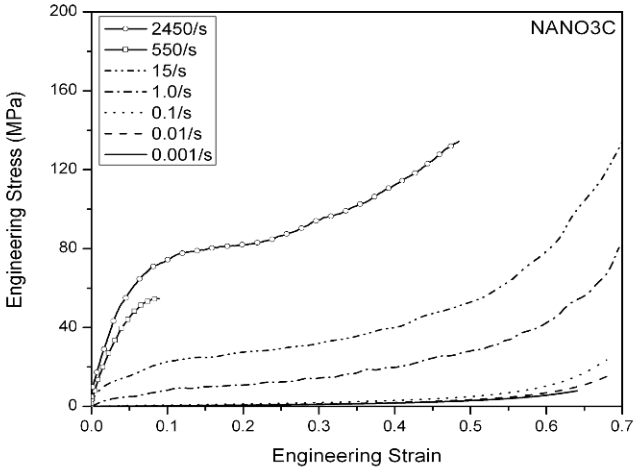


Figure 4.21 Compressive stress-strain curves of ESO/Clay-0
*(Reproduced from Song et al. (2006a) with permission)*

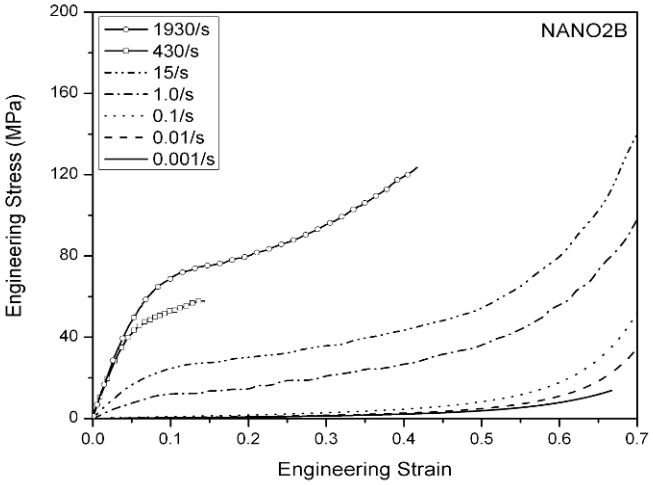


Figure 4.22 Compressive stress-strain curves of ESO/Clay-5
*(Reproduced from Song et al. (2006a) with permission)*

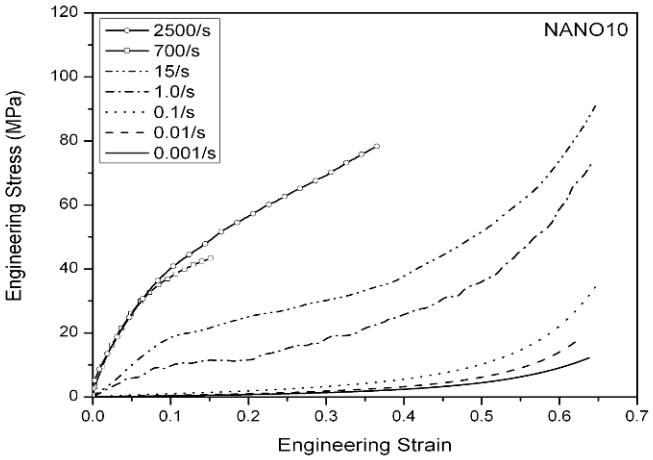


Figure 4.23 Compressive stress-strain curves of ESO/Clay-8
*(Reproduced from Song et al. (2006a) with permission)*

The effects of nanoclay on the strength of the nano-composite materials were found to be mixed. The nanoclay is shown to enhance the strength of the nanocomposites only at low strain rates. The addition of nanoclay has little or negative effects on the material stress at a certain strain and at high strain rates. When strain rate is below 1.0 $s^{-1}$, the stress at a certain strain increases with increasing nanoclay weight. At the strain rate of 1.0 $s^{-1}$, the stresses for both nanocomposites were still enhanced in comparison with that for the material without nanoclay. However, the stress for the composite with 5% nanoclay is superior to that for the composite with 8% nanoclay at this strain rate. When the strain rate is increased to 15 $s^{-1}$, the stress increases when the nanoclay addition up to 5% in weight. However, when more nanoclay (8%) is added, the stress becomes even lower than that for the material without nanoclay. At further higher strain rates, the material without nanoclay has the highest stress at small strains. At a certain strain level, the stress decreases with increasing weight of nanoclay. At large strains, the dynamic stress increases slightly when 5% weight nanoclay is added, but significantly decreases when more nanoclay (8%) is added. The experimental results indicate that the material containing too much nanoclay without special treatment damages its strength due to possible aggregation of the clay layers.

Table 4.3 Strain-rate and nanoclay-weight effects
*(Reproduced from Song et al. (2006a) with permission)*

| | ESO:H = 1:1.37 | | | | | |
|---|---|---|---|---|---|---|
| Components | ESO/clay-0 | | ESO/clay-5 | | ESO/clay-8 | |
| Nanoclay weight | 0 | | 5% | | 8% | |
| Strain | Strain rate ($s^{-1}$) | Stress (MPa) | Strain rate ($s^{-1}$) | Stress (MPa) | Strain rate ($s^{-1}$) | Stress (MPa) |
| 5% | $10^{-3}$ | 0.12 | $10^{-3}$ | 0.15 | $10^{-3}$ | 0.16 |
| | $10^{-2}$ | 0.19 | $10^{-2}$ | 0.23 | $10^{-2}$ | 0.26 |
| | $10^{-1}$ | 0.37 | $10^{-1}$ | 0.53 | $10^{-1}$ | 0.60 |
| | 15 | 15.62 | 15 | 16.60 | 15 | 10.07 |
| | 550 | 44.96 | 430 | 41.72 | 700 | 26.24 |
| | 2450 | 58.13 | 1930 | 48.22 | 2540 | 26.01 |
| 10% | $10^{-3}$ | 0.25 | $10^{-3}$ | 0.30 | $10^{-3}$ | 0.33 |
| | $10^{-2}$ | 0.34 | $10^{-2}$ | 0.43 | $10^{-2}$ | 0.48 |
| | $10^{-1}$ | 0.63 | $10^{-1}$ | 0.88 | $10^{-1}$ | 1.02 |
| | 15 | 22.63 | 15 | 24.76 | 15 | 18.65 |
| | 550 | / | 550 | 52.95 | 550 | 37.52 |
| | 2450 | 74.36 | 1930 | 68.93 | 2540 | 40.22 |
| 40% | $10^{-3}$ | 1.72 | $10^{-3}$ | 2.13 | $10^{-3}$ | 2.42 |
| | $10^{-2}$ | 1.94 | $10^{-2}$ | 2.62 | $10^{-2}$ | 3.22 |
| | $10^{-1}$ | 3.05 | $10^{-1}$ | 4.66 | $10^{-1}$ | 5.51 |
| | 15 | 39.83 | 15 | 43.35 | 15 | 37.72 |
| | 550 | / | 550 | / | 550 | / |
| | 2450 | 112.28 | 1930 | 119.02 | 2540 | 79.65 |

### 4.5.2.3 EPDM Rubber

An ethylene-propylene-diene monomer copolymer (EPDM) rubber was characterized with the same procedure in Kolsky compression bar experiments. Here we present the resultant stress-strain behavior for the EPDM rubber at various strain rates.

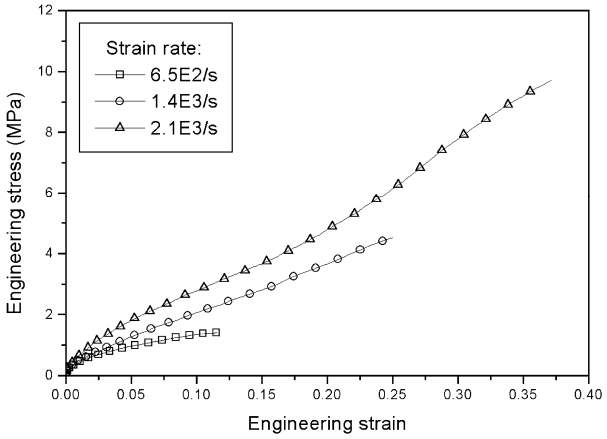


(a)

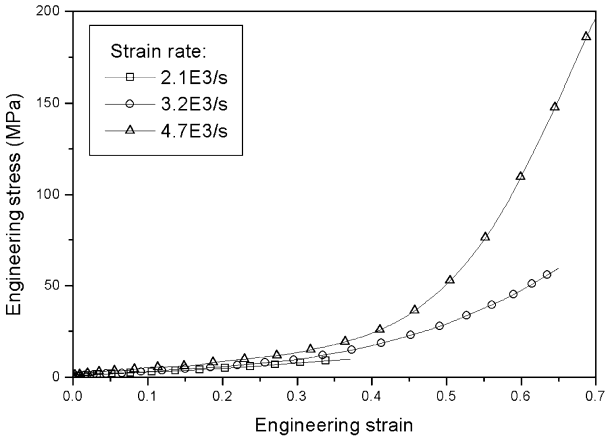


(b)

Figure 4.24 Compressive stress-strain curves of EPDM rubber
*(Reproduced from Song and Chen (2003) with permission)*

Figure 4.24 shows the compressive engineering stress-strain curves for this EPDM rubber, which are grouped into two graphs due to the drastic stress amplitude differences at different strain rates. The dynamic stress-strain behavior of the EPDM rubber is highly nonlinear with significant strain-rate effects. For each stress-strain curve, the slope increases significantly with increasing strain at large strains (>5%), which is different from that at small strains (<5%). The strain rate sensitivity also depends on the amplitude of strain. The strain rate effect on the nonlinear mechanical response of the EPDM rubber has been quantitatively studied and modeled (Song and Chen 2003, Song et al. 2004a).

### 4.5.3 Foams

Foam materials exhibit unique mechanical response to external loading. Changes in the matrix material or cell structures (open or closed cell structures) can consequently result in significant change in their global material response. Generally, the foam materials may be classified into two groups: elastic-brittle foams and elastic-plastic foams according to their mechanical responses. Different types of foams may require different designs in Kolsky-bar experiments. In this section, we present the Kolsky-bar experiment designs for brittle and elastic-plastic foams, respectively.

#### 4.5.3.1 Brittle Foams

The material we present here is an epoxy syntactic foam, which is made of an epoxy resin as binder and hollow glass microspheres with a maximum diameter of 50 μm as fillers. This syntactic foam has a density of $0.77\times10^3$ kg/m$^3$, a glass transition temperature of 70°C, and an ultrasonic longitudinal wave speed of 2700 m/s. This longitudinal wave speed may not necessitate thin specimens for achieving stress equilibrium. The specimen has a thickness of 6.35 mm and a diameter of 12.70 mm, producing a length-to-diameter ratio of 0.5.

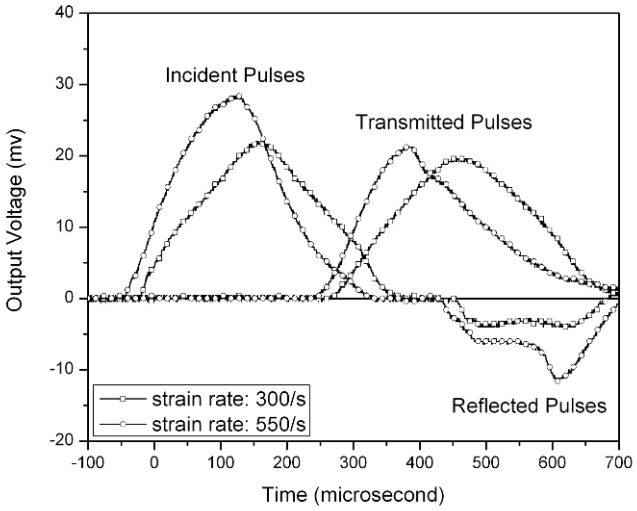


Figure 4.25 Kolsky bar experiments on epoxy syntactic foam

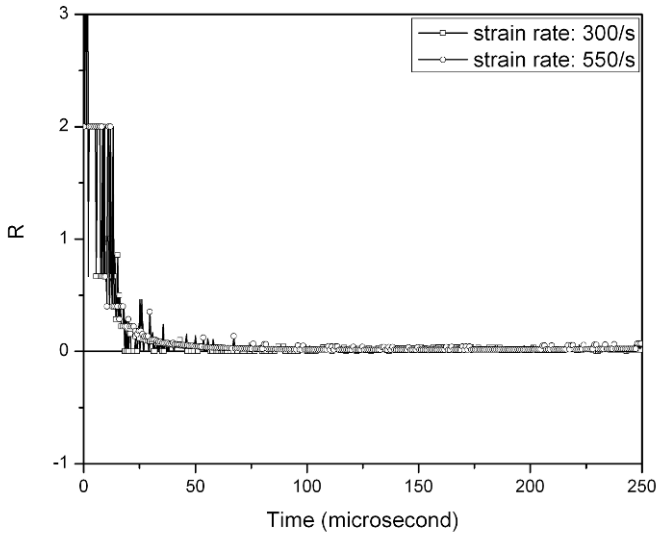


Figure 4.26 Dynamic stress equilibrium processes

The Kolsky bar schematically shown in Fig. 4.13 was employed for dynamic compression experiments. To facilitate a constant strain-rate deformation in such a nearly linear elastic material, a ramp loading pulse with a constant slope is necessary. This ramp slope determines the strain rate in the specimen. The ramp incident pulses with different slopes were produced with annealed C11000 copper disk pulse shapers of various dimensions associated with different striking velocities.

Figure 4.25 shows two sets of incident, reflected, and transmitted signals at the strain rates of 300 and 550 $s^{-1}$ (Song and Chen 2005). It is observed that, such nearly linear profiles of the incident pulses produced plateaus in the reflected pulses, which represent constant strain rates if the stress is proven to be in dynamic equilibrium. Figure 4.26 shows the processes of dynamic stress equilibrium by means of (4.5). The forces at both ends of the specimen were directly measured with the quartz-crystal force transducers (Fig. 4.13). The axial inertia force brought by the aluminum disk at the incident bar end is insignificant as compared to the strength of the syntactic foam, making it unnecessary to compensate this axial inertia force. Only single quartz crystal was used. It is observed that the specimens were in stress equilibrium within most of loading durations at both strain rates due to the modified loading profiles through pulse-shaping. The strain-rate histories in specimens are shown in Fig. 4.27. The strain rate does not reach constant values until ~50 μs after the specimen is loaded. When the strain rate is high, i.e., 550 $s^{-1}$ in Fig. 4.26, it may have a sharp rise following the constant part due to the sudden failure of the brittle specimen. This is similar mechanism to the brittle material characterization described in Chapter 3.

Figure 4.28 shows the dynamic compressive stress-strain curves of the epoxy syntactic foam over a range of strain rates from 300 to 1900 $s^{-1}$ (Song et al. 2004b). The elastic recovery in the stress-strain curve at 300 $s^{-1}$ is the result of unloading before reaching the failure of the specimen. The maximum stress shown in this curve does not represent the specimen failure strength. However, for the other stress-strain curves in Fig. 4.28, the peaks indicate the failure strength of the material. The sudden increase in the reflected signals in those experiments indicates that the specimens fail catastrophically during the first pass of the loading pulse. Both Young's modulus and failure strength increase when the strain rate increases from 300 to 550 $s^{-1}$. However, little change in both modulus and failure strength was observed when the strain rate further increases to 1030 $s^{-1}$. Moreover, both modulus and failure strength decrease when the strain rate reaches a higher level at 1900 $s^{-1}$. This puzzling phenomenon has been concluded as a result of mixture of strain-rate strengthening and damage softening in the specimen under dynamic loading. A strain-

rate- and damage-dependent material model has been developed to describe the phenomenon (Song et al. 2004b).

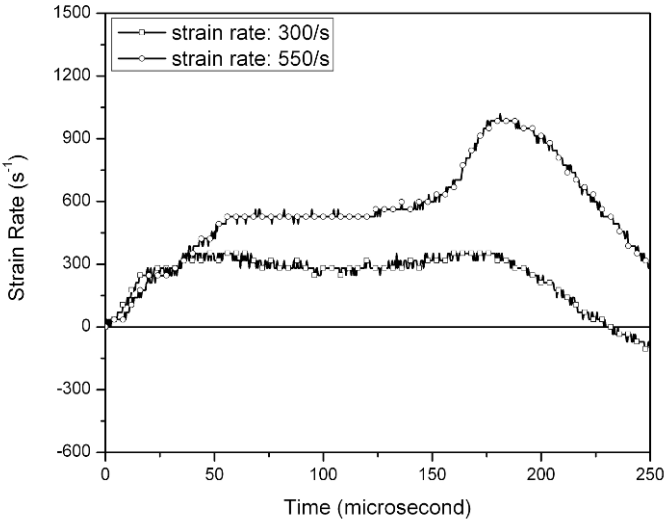


Figure 4.27 Strain-rate histories

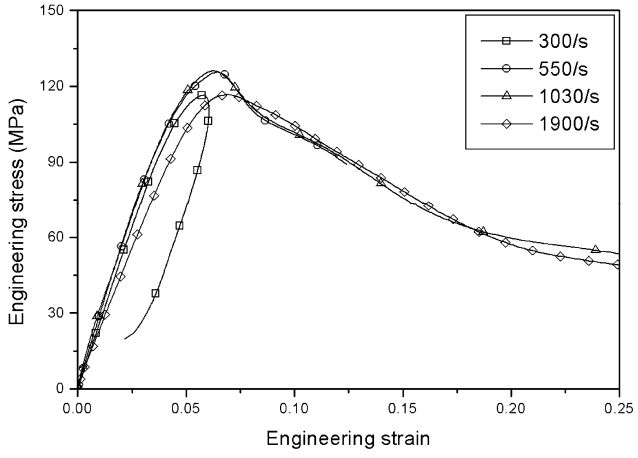


Figure 4.28 Compressive stress-strain curves of epoxy syntactic foam
*(Reproduced from Song et al. (2004b) with permission)*

### 4.5.3.2 Elastic-plastic Foam

Due to the significant differences in the transmitted signals between brittle foams and elastic-plastic foams, the pulse shaping design for testing elastic-plastic polymeric foams is different from that for testing brittle foam described above.

Elastic-plastic polymeric foams are unique in their compressive stress-strain curves: elastic, cell collapsing, and densification stages. In addition, the low mass density and slow wave speed in the elastic-plastic polymeric foams result in drastically reduced wave impedance. Consequently, nearly all of the incident pulse is reflected back and the transmitted pulse is hardly recorded by regular resistor strain gages. In other words, the transmitted pulse has a negligible amplitude as compared to the incident pulse. In this case, a trapezoidal incident pulse is needed to produce constant strain rate on the specimen. The rise time of the trapezoidal pulse should be sufficiently long to allow the specimen to achieve stress equilibrium. In Kolsky-bar experiments on low-density polymeric foams, stress equilibrium becomes a more challenging condition to meet than constant strain-rate deformation. The foam specimen could collapse progressively from one end to the other end if the pulse shaping and specimen length are not carefully designed (Song et al. 2006c). The low initial loading slope (or long rise time) allows the specimen to have sufficient time to achieve uniform stress during the early stages of loading, thereby giving the specimen a chance for uniform deformation. To facilitate such a trapezoidal incident pulse with a low initial slope, both copper tubes and copper disks have been found to be effective serving as pulse shapers. In addition, the foam specimen is required to be thin but still needs to contain several cells along the thickness direction to make an effective representative volume. Due to small Poisson's ratios in such foams before the deformation reaches densification stage, the effects of radial inertia and interfacial friction are negligible in the dynamic compression experiments on these foams.

Figure 4.29 shows the typical pulses obtained from a Kolsky compression bar experiment on a 3.3-mm-thick, 12.2-mm-diameter rigid polyurethane foam specimen using a copper tube as pulse shaper (Song et al. 2005b). The $0.24\times10^3$ kg/m$^3$ foam material has an average closed-cell size of 200 μm, possessing at least 16 cells along the 3.3-mm-thick direction. As shown in Fig. 4.29, the rise time of the modified incident pulse is approximate 50 μs which is about five times longer than that (~10 μs) in a conventional Kolsky-bar experiment. In addition, the weak

transmitted signal was sensed by semiconductor strain gages (Fig. 4.29). Note that the transmitted signal shown in Fig. 4.29 is measured with semiconductor strain gages that are about 70 times higher in sensitivity than resistor strain gages. The actual amplitude of the transmitted signal is much lower than the incident pulse. In hence, the hardening portion behind the stress plateau in the transmitted signal does not significantly affect the design of incident pulse for the purpose of achieving constant strain-rate deformation. The dynamic stress equilibrium process monitored with quartz-crystal force transducers is shown in Fig. 4.30. Even though the pulse shaper was employed to reduce the initial incident loading rate, the stress in the specimen was not equilibrated until 50 μs after initial loading, resulting in unreliable stress-strain data for the first 50 μs. The first 50 μs period produces approximate 12% strain at this strain rate (4100 $s^{-1}$), which is beyond yield strain for the foam.

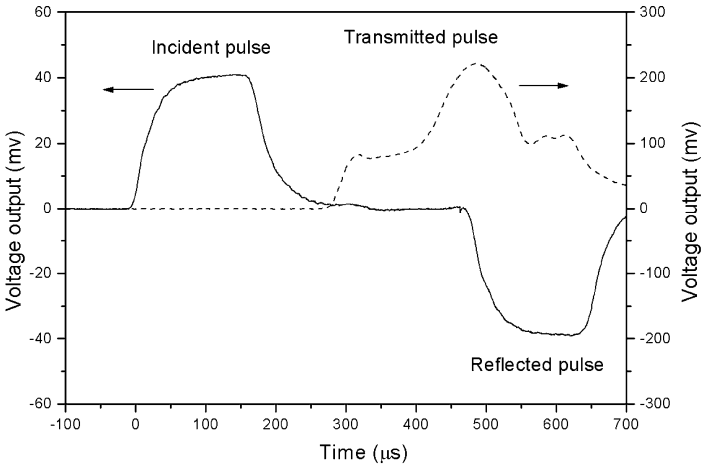


Figure 4.29 Kolsky bar experiment on a rigid polyurethane foam
*(Reproduced from Song et al. (2005b) with permission)*

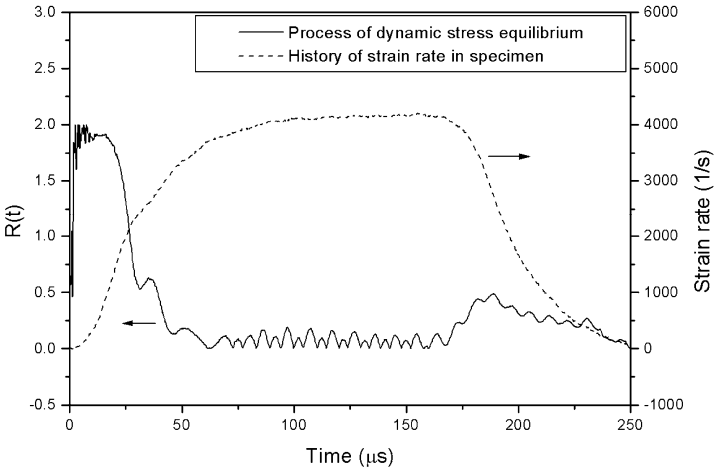


Figure 4.30 Dynamic stress equilibrium at the strain rate of 4100 $s^{-1}$
*(Reproduced from Song et al. (2005b) with permission)*

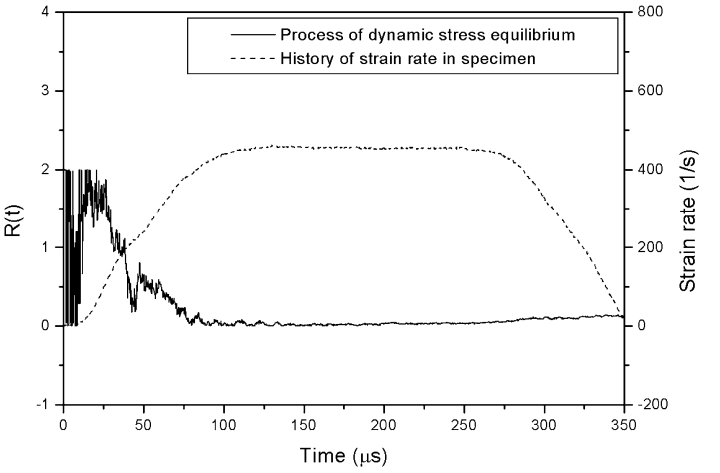


Figure 4.31 Dynamic stress equilibrium at the strain rate of 450 $s^{-1}$
*(Reproduced from Song et al. (2005b) with permission)*

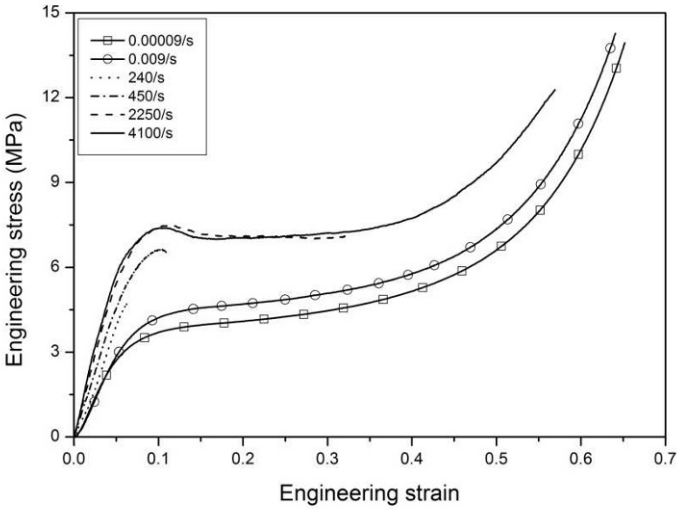


Figure 4.32 Compressive stress-strain curves of rigid polyurethane foam
*(Reproduced from Song et al. (2005b) with permission)*

In order to investigate the initial elastic and early collapse behavior of the material, the loading rate of the incident pulse needs to be further lowered. Under such loading pulses, the stress equilibrium in the specimen can be achieved at much earlier stages of the deformation, i.e., at strains much smaller than the 12% in the experiments described above. However, due to the focus on the initial stages of the experiment in design, the strain rate level will have to decrease inevitably such that the experiment does not rush through the initial states in the attempt to approach a higher strain rate. Figure 4.31 indicates that the stress equilibrium was achieved at 85 μs after initial loading, which corresponds to only 1.7% strain at the strain rate of 450 $s^{-1}$. As a result, most of the elastic portion and early collapse portion in the stress-strain curve for the foam material were obtained accurately under controlled testing conditions, but at relatively low strain rates.

Figure 4.32 shows the stress-strain curves of the polyurethane foam at various strain rates. The initial elastic and early cell-collapse data are not reliable for the experiments at the strain rates of 2250 and 4100 $s^{-1}$ but are accurate when the strain rate is down to 240 or 450 $s^{-1}$.

The elastic and early cell collapse response has also been investigated for a polystyrene foam with the Kolsky-bar techniques (Song et al. 2005a). The polystyrene foam material was manufactured under precise control of processing parameters to produce relatively uniform microstructures (Wischmann and Assink 1977). The global foam material had fused hexagonal interfaces among the conjoint polystyrene beads with open cells approximately 50-60 μm in diameter inside the closed foam beads. The $0.4\times10^3$ kg/m$^3$ density foam material was made into cylindrical specimens with a diameter of 12.70 mm, but 3.0 and 6.0 mm in thickness for Kolsky-bar and quasi-static experiments, respectively. The compressive stress-strain curves of the polystyrene foam are shown in Fig. 4.33. As presented in Chapter 2.7, there is an upper limit of constant strain rate to obtain reliable stress-strain response for elastic specimens including the elastic-brittle foams as well as the early elastic and cell-collapse response for the elastic-plastic foam.

Due to very similar elastic-plastic characteristic, the above Kolsky compression bar technique is applicable to many other polymeric foam materials. The mechanical response, however, may quantitatively differ from material to material because of variations in the matrix material, cell structure, density, and so on.

Figure 4.34 shows the compressive stress-strain curves of a removable epoxy foam with a low density of $0.12\times10^3$ kg/m$^3$ at various strain rates (Song et al. 2007c). This removable epoxy foam is designed to be cast in molding applications but can be removed with mild solvent at 90ºC to allow for recovery of potted components when used as a potting material. The epoxy foam has a closed cell structure with an average cell size of ~200 μm in diameter. The epoxy foam specimen for Kolsky compression bar experiments had a diameter of 13.80 mm and a thickness of 2.70 mm. The high-rate stress-strain curves were experimentally obtained with the Kolsky-bar experiments following the same procedure as above. This removable epoxy foam exhibits similar stress-strain response of elasticity-plastic plateau-densification hardening stages, but with a lower cell-collapsing stress (plastic plateau) of approximately only 1 MPa. The plateau stress increases with increasing strain rate.

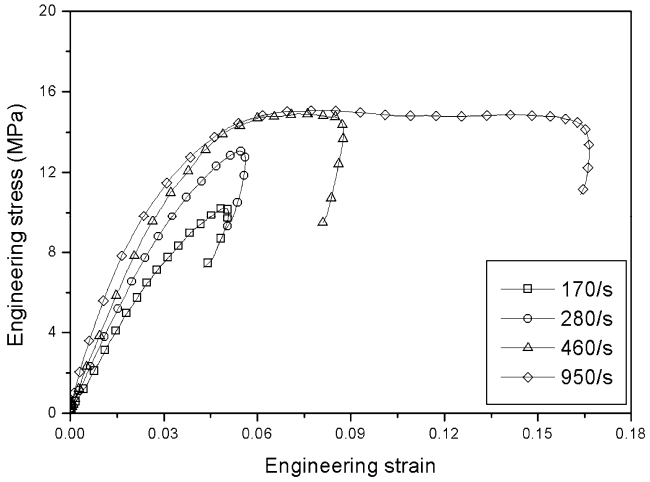


Figure 4.33 Elastic and early collapse response of polystyrene foam
*(Reproduced from Song et al. (2005a) with permission)*

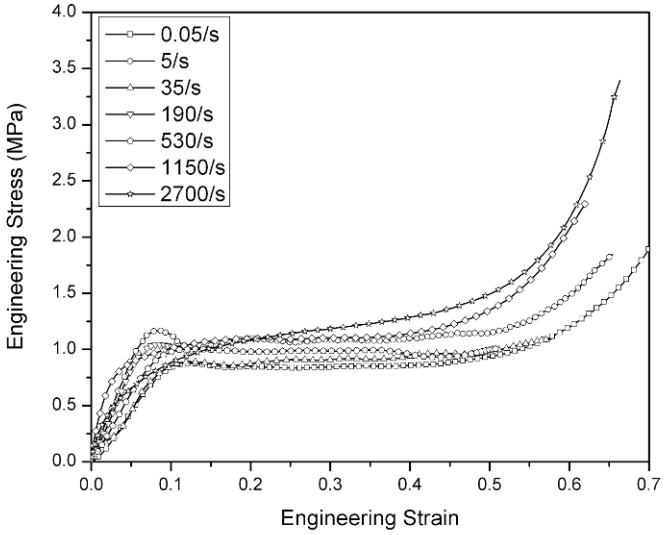


Figure 4.34 Compressive stress-strain curve of $0.12\times10^3$ kg/m$^3$ epoxy foam
*(Reproduced from Song et al. (2007c) with permission)*

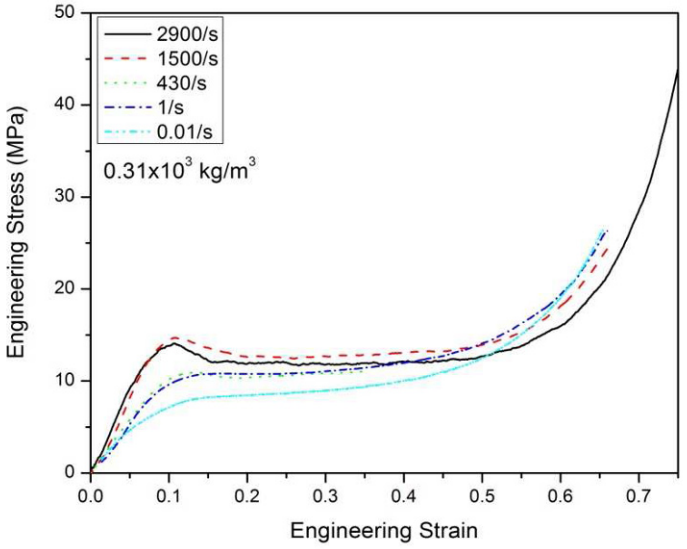
2900/s
1500/s
430/s
1/s
0.01/s
0.31x10^3 kg/m^3
Engineering Stress (MPa)
Engineering Strain
0
10
20
30
40
50
0.0
0.1
0.2
0.3
0.4
0.5
0.6
0.7

(a)

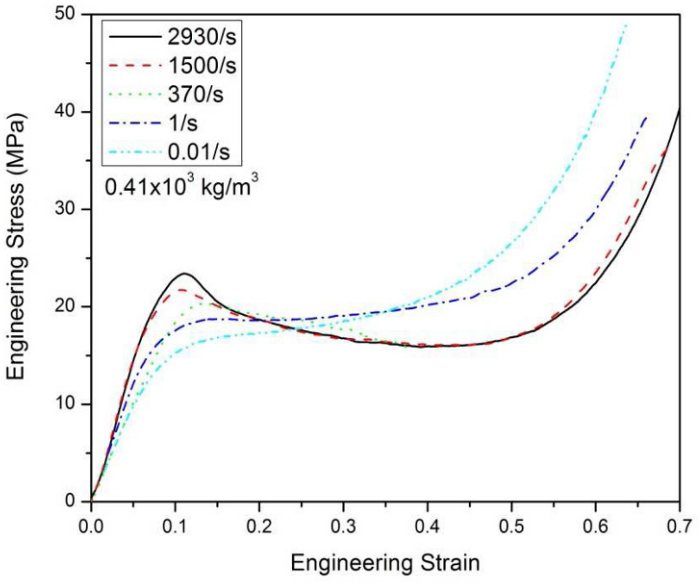
2930/s
1500/s
370/s
1/s
0.01/s
0.41x10^3 kg/m^3
Engineering Stress (MPa)
Engineering Strain
0
10
20
30
40
50
0.0
0.1
0.2
0.3
0.4
0.5
0.6
0.7

(b)

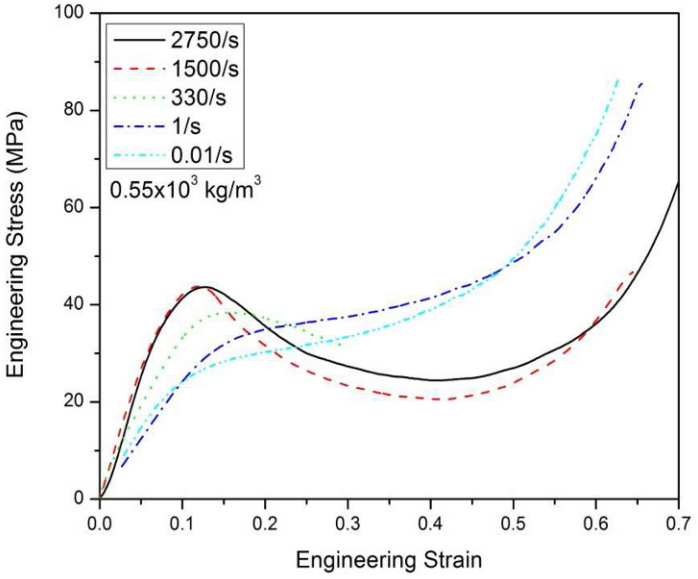


(c)

Figure 4.35 Compressive stress-strain curves of PMDI foam
*(Reproduced from Song et al. (2009d) with permission)*

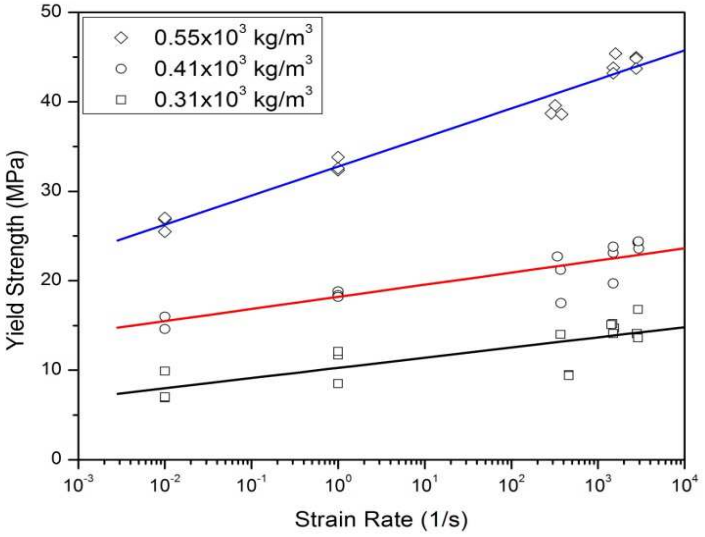


Figure 4.36 Effects of strain rate and density on compressive response of the PMDI foam
*(Reproduced from Song et al. (2009d) with permission)*

Foam density has been found to be a key parameter dominating the mechanical response. Figure 4.35 shows the compressive stress-strain response of a polymethylene diisocyanate (PMDI) based rigid polyurethane foam with three different densities ($0.31\times10^3$, $0.41\times10^3$, and $0.55\times10^3$ kg/m$^3$) at various strain rates (Song et al. 2009d). The PMDI foam materials have a closed-cell structure with a cell diameter varying from 100 to 200 μm. The foam densities were produced by controlling the volume fraction of the cells. Besides the strain-rate effect, density also significantly affects the mechanical response, i.e., yield strength, of the foam materials, as shown in Fig. 4.36. For a foam material with a certain density, the yield strength linearly increases with the logarithm of strain rate. Furthermore, at a certain strain rate, the yield strength significantly increases with increasing foam density.

## 4.5.4 Biological Tissues

The Kolsky bar experimental technique for the engineered soft materials presented in previous sections has also been applied for dynamic characterization of soft biological tissues. In this section, we present experiments on muscles and brain tissues.

### 4.5.4.1 Porcine Muscles

Porcine muscles have similar issues as other soft materials under Kolsky bar loading in terms of inertia effects, interfacial friction and dynamic equilibrium. Therefore, thin specimens are necessary for axial stress equilibrium, hollow geometry is necessary to minimize radial inertia effects, the interfaces between the specimen and the bar ends need to be properly lubricated, and pulse shaping is needed to facilitate constant strain rate under dynamic equilibrium.

Unlike working with engineered materials, attention is paid to the specimen conditions when the biological tissues are subject to mechanical loading. For example, in order to closely simulate the actual response of “live” tissues in applications, the biological tissues need to remain “fresh” when subjected to mechanical loading. To preserve the tissues investigated in the porcine muscle examples given here, a modified Kreb

solution (136 m*M* NaCl, 4 m*M* KCl, 2.35 m*M* $CaCl_2$, 1 m*M* $NaH_2PO_4$, 0.85 m*M* $MgCl_2$, 12 m*M* $NaHCO_3$, 5 m*M* glucose, PH=7.4) bubbled with 95% $O_2$ and 5% $CO_2$ at the temperature of 39.2°C (López et al. 1988) was used.

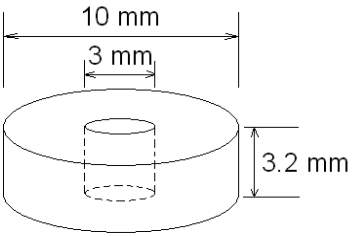


(a)

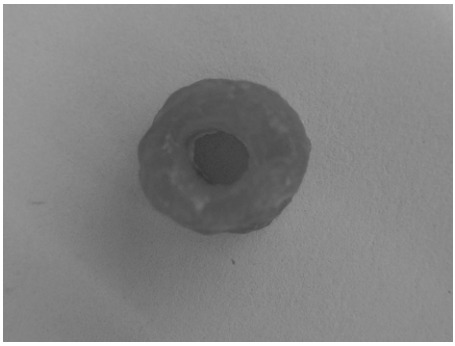

(b)

Figure 4.37 Schematic and photograph of annular porcine muscle tissue
*(Reproduced from Song et al. (2007b) with permission)*

The muscle tissues from a ham of a 5-month-old female swine have been characterized with the loading direction along and perpendicular to the fiber direction by using the Kolsky-bar techniques modified for soft material characterization (Song et al. 2007b). Immediately after the slaughter, the ham of the swine was marinated in the modified Kreb solution and then sliced into 3.2-mm-thick flat sheets along and perpendicular to fiber directions. The flat sheets were cut with 10.0-mm- and 3.0-mm-diameter trephine blades with sharp edges (to minimize damage to the neighboring tissues during cutting) to make annular tissue specimens with 10.0-mm outer diameter and 3.0-mm inner diameter for dynamic experiments. Figure 4.37 shows the schematic and photograph of the annular specimen. The annular specimen is not necessary for quasi-static experiments because the radial inertia is negligible when the loading rate is low. Conventional solid disk specimens with 3.2-mm in thickness and 10.0-mm in diameter were used for quasi-static experiments. The low strength of the soft tissue requires sufficient lubrication on the specimen ends. Vegetable oil was found to be excellent in lubricating soft biological tissues.

Due to extremely low strength in the biological tissues, the trapezoidal incident pulse is capable of producing constant strain rate deformation. However, the rise time should be sufficiently long to achieve dynamic stress equilibrium in such soft tissue specimens. In addition, the high-frequency oscillations that usually appear in conventional incident pulses should be eliminated. Such oscillations are significant enough to disturb the loading conditions on the tissue specimen with a very low strength. Either annealed copper disk or tube can serve as an effective pulse shaper.

The incident, reflected, and transmitted pulses from a typical high-rate experiment on the porcine muscle are shown in Fig. 4.38. It is observed that the spike appeared in the transmitted pulse in Fig. 4.4 disappeared in Fig. 4.38 after annular specimen geometry and proper pulse shaping were employed. The radial inertia has been minimized. This pulse shaping also minimizes the axial inertia, which was verified by comparing the forces measured with the quartz crystal force transducers at both ends of the specimen (Fig. 4.39). The axial inertia in the aluminum disk on top of the quartz crystals has been compensated by using three quartz transducers. The stress measurement by the quartz crystals may still contain noise-like oscillations in the loading histories due to the small amplitudes of the pulses. Figure 4.40 shows the strain rate and strain histories in the specimen indicating that the specimen deformed at a nearly constant strain rate of 3650 $s^{-1}$.

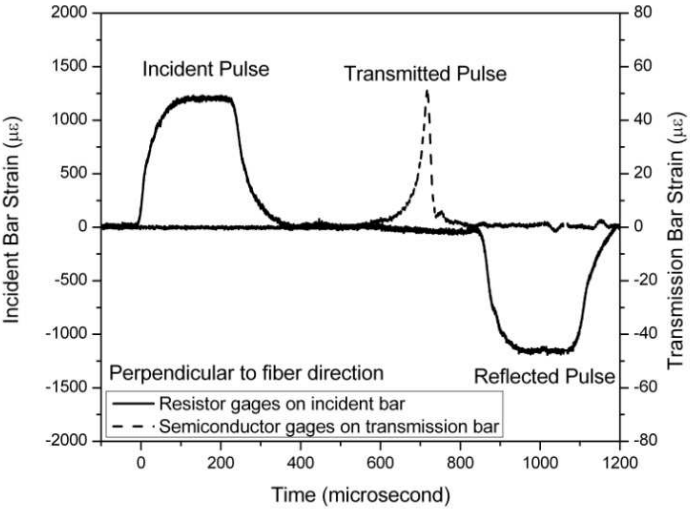


Figure 4.38 Kolsky bar experiment on porcine muscle tissue
*(Reproduced from Song et al. (2007b) with permission)*

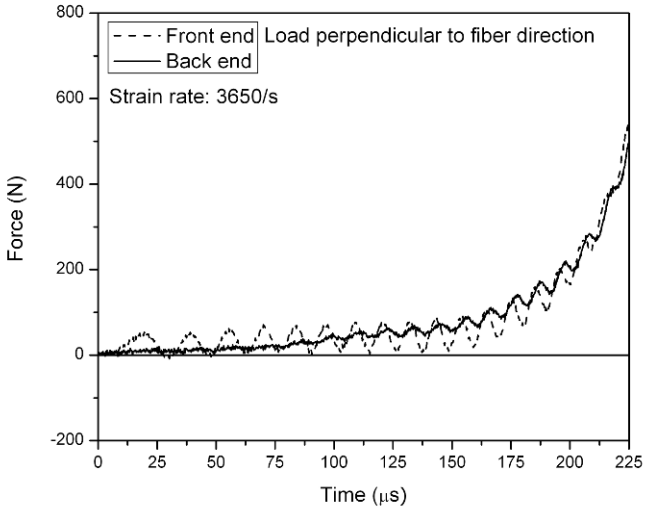


Figure 4.39 Stress equilibrium in the porcine muscle tissue specimen
*(Reproduced from Song et al. (2007b) with permission)*

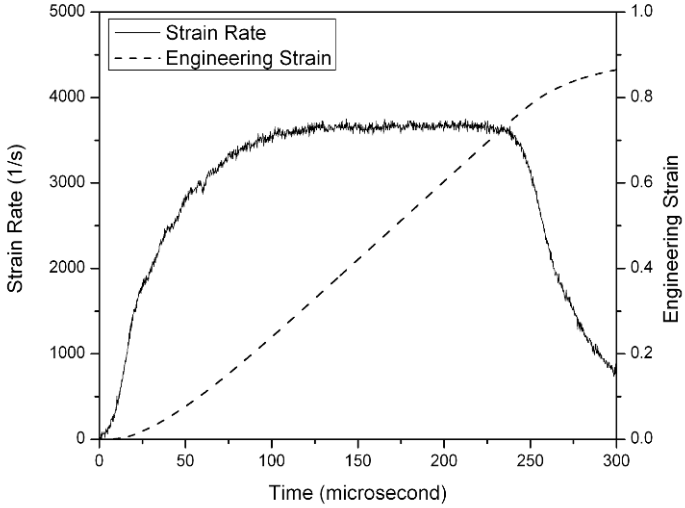


Figure 4.40 Strain rate and strain histories in the porcine muscle tissue specimen
*(Reproduced from Song et al. (2007b) with permission)*

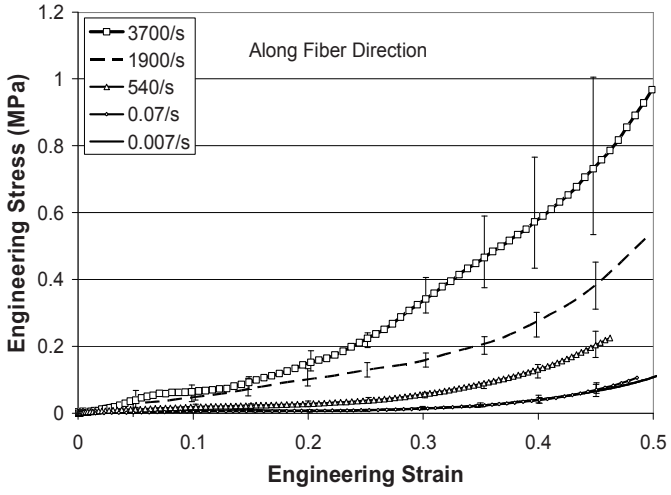


Figure 4.41 Compressive stress-strain curves of the porcine muscle tissue where loading is perpendicular to the fiber direction
*(Reproduced from Song et al. (2007b) with permission)*

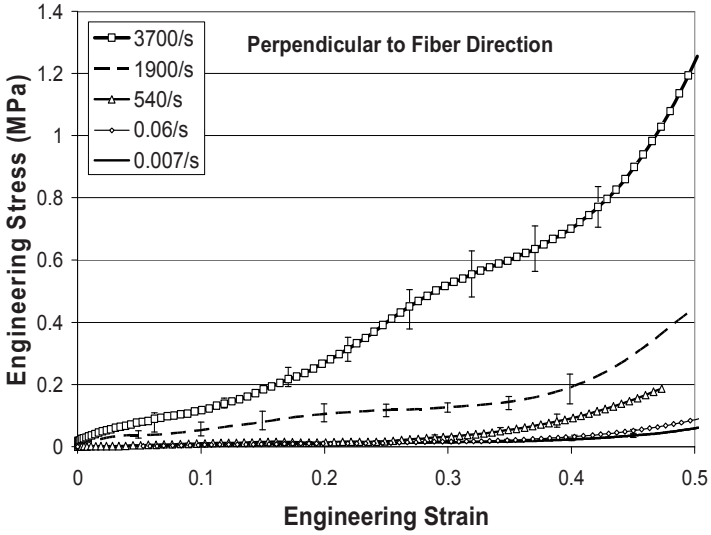


Figure 4.42 Compressive stress-strain curves of the porcine muscle tissue where loading is along the fiber direction
*(Reproduced from Song et al. (2007b) with permission)*

Figures 4.41 and 4.42 show the resultant compressive stress-strain curves of the porcine muscle tissues where the loading direction is along and perpendicular to the muscle fiber direction, respectively. In both Figs. 4.41 and 4.42, error bars were plotted on the mean stress-strain curves from several repeated experiments to show the level of data scatter under identical testing conditions. Regardless of loading direction, the stress-strain curves exhibit rubber-like mechanical characteristic: a toe region at the beginning, followed by a transitional non-linear response and then a strain-hardening behavior. Strain-rate effects are apparent in the porcine muscle tissue. However, the strain-rate sensitivity depends on the loading direction. The strain-rate sensitivity along the perpendicular direction is more significant than that along the fiber direction.

### 4.5.4.2 Brain Tissues

Similar experimental setup for the porcine muscle experiments was used to determine the dynamic responses of brain tissues (Pervin and Chen 2009). Using a similar experimental facility, the gray and white matters of fresh bovine brain tissues were characterized under compression to large strains over a strain rate range from 0.01 to 1800 $s^{-1}$. The white matter was examined both along and perpendicular to the coronal section for anisotropy characterization. Similar to the practice in porcine muscle experiments, a pulse shaper at the impact end of the incident bar is attached with vacuum grease to generate an initial ramp followed by a plateau to facilitate early dynamic stress equilibrium and constant strain rate in the specimen. However, the impact of the striker is at much lower velocities. In order to increase the amplitude of the transmitted signal from soft brain tissues, a hollow aluminum transmission bar was used, together with semiconductor strain gages on the transmission bar. Quartz-crystal force transducers were used to verify the dynamic equilibrium in the specimen. The transducer on the incident bar end has a three-quartz configuration to compensate the inertia brought by the introduction of the aluminum disk.

The experiments for this study were performed *in vitro* on bovine brain. The brain from a twenty-one-months-old steer was collected from a slaughter house a few minutes after the death of the animal. The tissue was preserved in artificial cerebrospinal fluid at 37°C. All the experiments were completed within eight hours postmortem. Annular specimens of outer diameter 10 mm, inner diameter 4.7 mm and thickness 1.7 mm were excised from sections of gray matter (frontal and parietal lobe) and white matter (corona radiata). The geometry of the specimens is the same as the muscle specimen shown in Fig. 4.37 except for the dimensional differences in thickness and inner radius. A thin layer of vegetable oil was applied on the interface between the specimen and bar end face to minimize friction. A thickness gage was used to set the specimen initial thickness individually to eliminate pre-stressing the specimen before dynamic loading.

The incident, reflected, and transmitted strain signals of a typical Kolsky-bar experiment on brain tissues at a strain rate of 1800 $s^{-1}$ are shown in Fig. 4.43. The stress histories at the both end faces of the tissue specimen were measured by the quartz-crystal force transducers and compared for each experiment. The force histories were found to overlap

each other indicating dynamic equilibrium across the specimen thickness, as shown in Fig. 4.44.

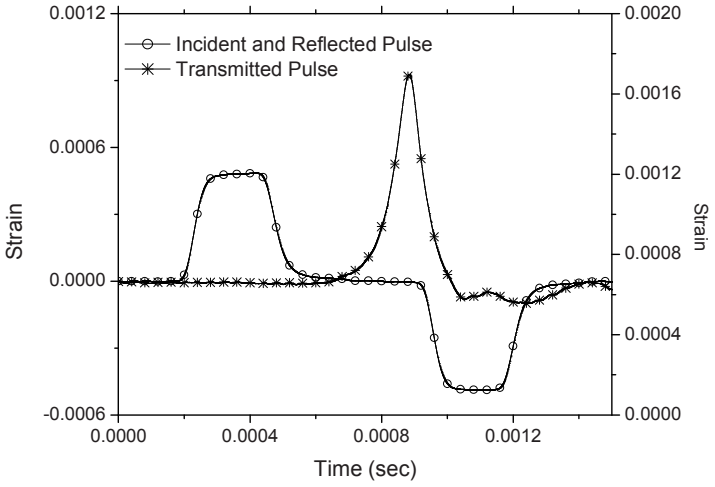


Figure 4.43 Strain signals from a Kolsky bar experiment on a brain tissue specimen
*(Reproduced from Pervin and Chen (2009) with permission)*

The resultant compressive stress-strain curves obtained on both gray and white matters are shown in Fig. 4.45. Due to significant difference in stress amplitude under quasi-static and dynamic loading, Fig. 4.45(a) shows the quasi-static stress-strain curves while dynamic stress-strain responses for both gray and white matters are shown in Fig. 4.45(b). Figure 4.45(a) also presents previous data for swine brain obtained by Miller and Chinzei (1997) for comparison purpose. For each strain rate, five experiments were repeated under the identical testing conditions. The results presented in Fig. 4.45 are mean data from 15 resultant data under identical testing conditions. Both gray and white matters exhibit similar characteristics: non-linear response with significant strain rate effects.

The stiffness significantly increases with increasing strain-rate. The mechanism behind the apparent rate effects is not completely understood. One possible factor is the change in damage/failure modes as the strain rate increases. Another possibility is the change in stress state under high rate loading due to the restrictions to the lateral motion of the soft brain tissue by radial inertia and/or friction. More experiments under other loading conditions need to be conducted to develop a comprehensive understanding of the behavior.

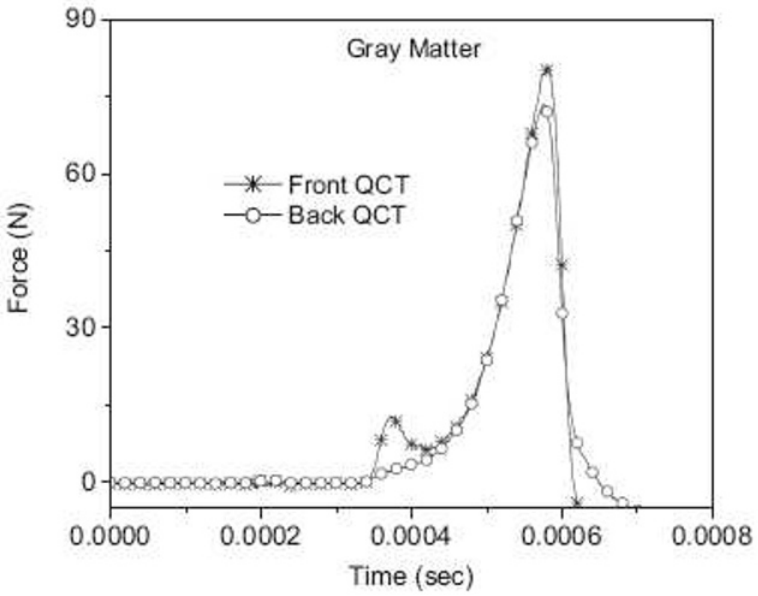


Figure 4.44 Dynamic stress equilibrium
*(Reproduced from Pervin and Chen (2009) with permission)*

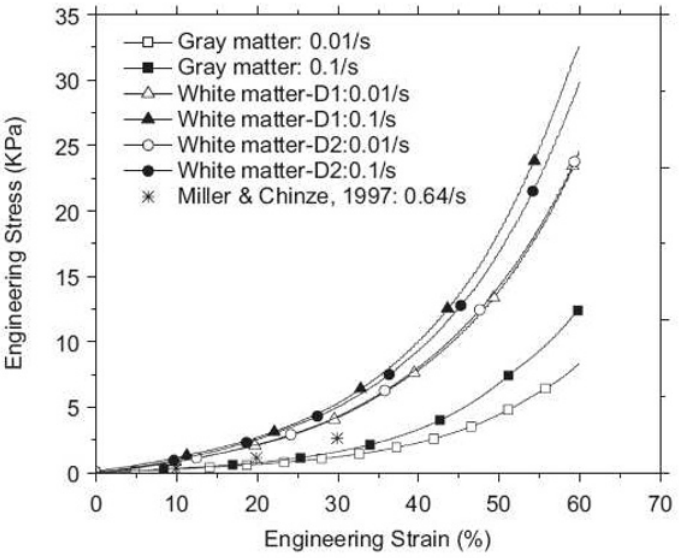


(a)

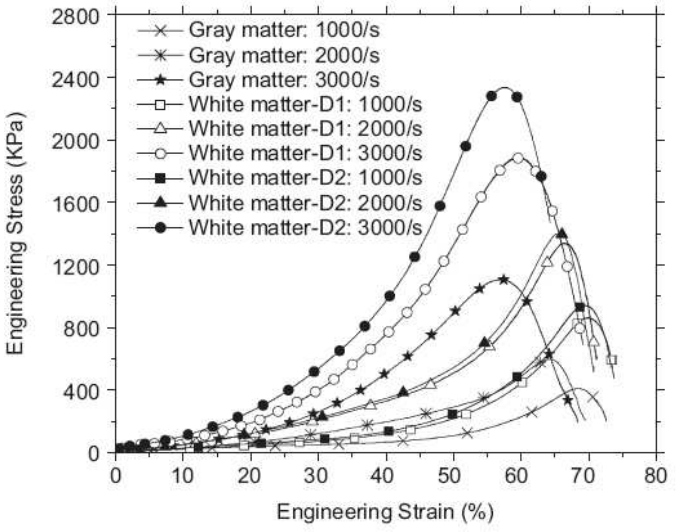


(b)

Figure 4.45 Compressive stress-strain curves of bovine brain tissues under (a) quasi-static and (b) dynamic loading conditions
*(Reproduced from Pervin and Chen (2009) with permission)*